

ABSTRACT

Title of Document:

TEST METHODOLOGIES FOR DYNAMIC FRACTURE STRENGTH OF SINGLE CRYSTAL SILICON

Saifa Hasin
Master of Science, 2008

Directed By:

Professor Donald Barker
Department of Mechanical Engineering

Single crystal silicon (SCSi) is the primary component for many microelectromechanical systems (MEMS). Therefore, identification of the dynamic fracture strength of SCSi can tremendously aid in virtual qualification of new MEMS devices used in dynamic loading applications. Unfortunately, the fracture strength is influenced by surface flaws, which are functions of microfabrication processing techniques. This work assesses the influence of deep reactive ion etching (DRIE) technology on the dynamic fracture strength of SCSi.

The primary focus was to develop test methodologies that can be used for identifying the dynamic fracture strength of SCSi. The methodologies developed were applied to simple MEMS shock test structures to measure preliminary dynamic fracture strength values. Based on the experiments performed thus far, the dynamic fracture strength of DRIE processed (100) SCSi is >1.10 GPa and <1.37 GPa for bending around $\langle 100 \rangle$ and $\langle 110 \rangle$ directions, respectively. A statistically significant number of tests will be performed in the near future for verifying these fracture strength values and quantifying the uncertainties. Finally, recommendations are provided for the planned future experiments.

TEST METHODOLOGIES FOR DYNAMIC FRACTURE STRENGTH OF
SINGLE CRYSTAL SILICON

By

Saifa Hasin

Thesis submitted to the Faculty of the Graduate School of the
University of Maryland, College Park, in partial fulfillment
of the requirements for the degree of
Master of Science
2008

Advisory Committee:
Professor Donald Barker, Chair
Professor Abhijit Dasgupta
Assistant Professor Sarah Bergbreiter

© Copyright by
Saifa Hasin
2008

Acknowledgements

I would like to thank my advisor, Dr. Donald Barker, for the encouragement, guidance, and patience he always offered me throughout my time as a graduate student at UMD.

Thanks are also due to Dr. Nathan Blattau of DfR Solutions and Mr. Morris Berman of the US Army Research Laboratory for providing access to the drop tower systems used to conduct the tests and to Mr. Thomas Loughran at the UMD FabLab for allowing me to use the teaching lab cleanroom for preparing the test samples. Additionally, I would like to thank Ms. Rachel Emmel, a co-investigator, for her help with various aspects of the project and Ms. Lyudmyla Panashchenko for showing me many different features on the ESEM.

I would also like to acknowledge the sponsorship of the CALCE Consortium, for providing research funding, and QinetiQ, for identifying the CALCE project as a critical project and for designing and building the MEMS structures that were tested during this research program.

Table of Contents

ACKNOWLEDGEMENTS	ii
TABLE OF CONTENTS	iii
LIST OF TABLES	v
LIST OF FIGURES	vi
CHAPTER 1: INTRODUCTION.....	1
CHAPTER 2: LITERATURE REVIEW.....	4
CHAPTER 3: DEVELOPMENT OF TEST METHODOLOGIES.....	11
SELECTION OF DYNAMIC TESTING METHOD	11
DESCRIPTION OF DEVICES	15
SAMPLE PREPARATION	17
HIGH ACCELERATION TESTING	18
STRUCTURAL FAILURE INSPECTION	20
FINITE ELEMENT ANALYSES AND SHOCK RESPONSE	21
SUMMARY	25
CHAPTER 4: APPLICATION OF TEST METHODOLOGIES	26
DESCRIPTION OF DEVICES	26
MAXIMUM STRESS DETERMINATION.....	29
DYNAMIC TESTING METHODOLOGY	30
TESTING RESULTS	32
DISCUSSION.....	38
CHAPTER 5: CONCLUSION.....	43

RECOMMENDATIONS FOR FUTURE WORK	46
APPENDIX A: ACCELEROMETER DRAWINGS.....	48
APPENDIX B: 4G SWITCH	53
APPENDIX C: ANALYTICAL STRESS CALCULATIONS.....	55
ANALYTICAL CALCULATIONS FOR BLOCK 1 TEST STRUCTURES	55
Axial Loading (Acceleration Along Positive X Direction).....	55
In-Plane Bending (Acceleration Along Negative Y Direction)	57
Out-of-Plane Bending (Acceleration Along Positive Z Direction).....	60
ANALYTICAL CALCULATIONS FOR BLOCK 2 TEST STRUCTURES	63
Axial Loading (Acceleration Along Positive X Direction).....	63
In-Plane Bending (Acceleration Along Negative Y Direction)	65
Out-of-Plane Bending (Acceleration Along Negative Z Direction)	70
ANALYTICAL CALCULATIONS FOR BLOCK 3 TEST STRUCTURES	72
Axial Loading (Acceleration Along Positive X Direction).....	72
In-Plane Bending (Acceleration Along Negative Y Direction)	74
Out-of-Plane Bending (Acceleration Along Negative Z Direction)	78
APPENDIX D: SHOCK AMPLIFICATION FACTOR CALCULATIONS.....	81
REFERENCES.....	83

List of Tables

TABLE 1: FRACTURE STRENGTH VALUES FOR BI-AXIAL FLEXURAL SAMPLES [11].	7
TABLE 2: FRACTURE STRENGTH VALUES FOR RADIUSED HUB FLEXURAL SAMPLES [11].	7
TABLE 3: SPECIMEN DIMENSIONS, WEIBULL PARAMETERS, AND BENDING STRENGTH FOR SCSi BEAMS OF VARIOUS SIZE SCALES [16] - [17].	9
TABLE 4: SUMMARY OF DROP TOWER TESTING.	19
TABLE 5: MODE SHAPES AND NATURAL FREQUENCIES OF 50G, 250G, AND 1000G ACCELEROMETERS	22
TABLE 6: SHOCK PARAMETER VALUES OF THE 50G, 250G AND 1000G ACCELEROMETERS FOR 2000G AND 5000G DROP TESTS	24
TABLE 7: WORST-CASE ESTIMATES OF DYNAMIC STRESS FOR SHOCK TEST STRUCTURES SUBJECTED TO ACCELERATION PULSES (3000G AND 5000G) ALONG CRITICAL LOADING DIRECTIONS	29
TABLE 8: DROP TOWER TESTING SUMMARY	32
TABLE 9: FAILURE SUMMARY OF BLOCK 2 AND BLOCK 3 SHOCK TEST STRUCTURES SUBJECTED TO 5000G DROP TESTS	33
TABLE 10: THE FIRST NATURAL FREQUENCY OF BLOCK 2 AND BLOCK 3 STRUCTURES	39
TABLE 11: SHOCK PARAMETER OF BLOCK 1, BLOCK 2, AND BLOCK 3 STRUCTURES	41
TABLE 12: SHOCK AMPLIFICATION FACTORS AND ACTUAL DYNAMIC STRESS VALUES FOR SHOCK TEST STRUCTURES SUBJECTED TO 3000G AND 5000G DROP TESTS	41
TABLE 13: MAXIMUM STRESS AND DISPLACEMENT FOR CANTILEVERS OF VARIOUS LENGTHS L	67
TABLE 14: MAXIMUM STRESS AND DISPLACEMENT FOR CANTILEVERS OF VARIOUS LENGTHS L	70
TABLE 15: MAXIMUM STRESS AND DISPLACEMENT FOR CANTILEVERS OF VARIOUS LENGTHS L	76
TABLE 16: MAXIMUM STRESS AND DISPLACEMENT FOR CANTILEVERS OF VARIOUS LENGTHS L	78
TABLE 17: STATIC STRESS SUMMARY FOR THE MEMS SHOCK TEST STRUCTURES	80
TABLE 18: SHOCK AMPLIFICATION FACTOR CALCULATIONS	82

List of Figures

FIGURE 1: WEIBULL PLOTS OF BENDING STRENGTH FOR VARIOUS SIZE SCALE SCSI BEAMS [16] - [17]	9
FIGURE 2: A RAIL GUN TESTING SYSTEM [21].....	12
FIGURE 3: AN AIR GUN SYSTEM [21]	13
FIGURE 4: A SPLIT HOPKINSON PRESSURE BAR SCHEMATIC [22].....	13
FIGURE 5: A LANSMONT DROP TOWER [23].....	14
FIGURE 6: A DETAILED VIEW OF A 1000G ACCELEROMETER DIE LAYOUT	16
FIGURE 7: A COMPARISON OF 50G, 250G AND 1000G SPRING GEOMETRIES	17
FIGURE 8: MEMS SPECIMEN FIXTURE.....	18
FIGURE 9: ACCELERATION PROFILES OF DROP TOWER TESTS	20
FIGURE 10: BEFORE AND AFTER ESEM OF A 50G ACCELEROMETER SUBJECTED TO A 1800 G DROP TEST	21
FIGURE 11: THE FIRST PRINCIPAL STRESS OF A 50G ACCELEROMETER WITH A PAIR OF MOVING FINGERS	23
FIGURE 12: DETAILED VIEW OF THE FIRST PRINCIPAL STRESS OF A 50G ACCELEROMETER WITH A PAIR OF MOVING FINGERS.....	23
FIGURE 13: SHOCK RESPONSE PARAMETER RELATIONS [28]	24
FIGURE 14: MASK LAYOUT OF THE MEMS SHOCK TEST STRUCTURES	27
FIGURE 15: A REPRESENTATIVE SHOCK TEST STRUCTURE FROM EACH BLOCK TYPE (NOT TO SCALE).....	27
FIGURE 16: MAXIMUM STRESS LOCATIONS FOR BLOCK 1, BLOCK 2, AND BLOCK 3 STRUCTURES.....	30
FIGURE 17: A MEMS SPECIMEN FIXTURE WITH TWO DIES (A BLOCK 2 AND A BLOCK 3) MOUNTED ON THE SIDE FOR SUBJECTING THE SHOCK TEST STRUCTURES TO IN-PLANE BENDING MOTION.....	31
FIGURE 18: ACCELERATION PROFILES OF A 3000G DROP TEST (TOP) AND A 5000G DROP TEST (BOTTOM)	31
FIGURE 19: ESEM IMAGES OF A BLOCK 2 DIE (LEFT) AND A BLOCK 3 DIE (RIGHT) THAT WERE SUBJECTED TO A 5000G ACCELERATION PULSE WITH AN IMPAC 66 VERTICAL SHOCK MACHINE.....	33
FIGURE 20: ESEM IMAGES OF STREAK MARK ETCHING ANOMALIES FOUND IN THE SHOCK TEST STRUCTURES	35
FIGURE 21: AN ESEM IMAGE OF WAVY ETCHING ANOMALIES FOUND IN THE SHOCK TEST STRUCTURES.....	35
FIGURE 22: ESEM IMAGES OF STRUCTURAL FAILURES OF MEMS SHOCK TEST STRUCTURES.....	36

FIGURE 23: ESEM IMAGES OF A BLOCK 1 DIE (LEFT) AND A BLOCK 3 DIE (RIGHT) THAT WERE SUBJECTED TO A 3000G ACCELERATION PULSE WITH A LANSMONT SHOCK TESTER.....	36
FIGURE 24: ESEM IMAGES OF STRUCTURAL FAILURES OF BLOCK 1 SHOCK TEST STRUCTURES	37
FIGURE 25: COMPLETE TIME HISTORY PLOT OF A 5000G DROP TEST	39
FIGURE 26: FFT OF TIME HISTORY PLOT SHOWING PEAKS AT 9.57 KHZ, 10.64 KHZ, AND 12.34 KHZ	40
FIGURE 27: A DETAILED VIEW OF A 4G SWITCH DIE.....	54
FIGURE 28: FIB CUT OF THE TETHER FREES THE PROOF MASS PRIOR TO TESTING	54
FIGURE 29: A BLOCK 1 TEST STRUCTURE AND ITS FREE BODY DIAGRAM (AXIAL LOADING).....	55
FIGURE 30: A BLOCK 1 TEST STRUCTURE AND ITS FREE BODY DIAGRAM (IN-PLANE BENDING).....	57
FIGURE 31: A BLOCK 1 TEST STRUCTURE AND ITS FREE BODY DIAGRAM (OUT-OF-PLANE BENDING)	60
FIGURE 32: A BLOCK 2 TEST STRUCTURE AND ITS FREE BODY DIAGRAM (AXIAL LOADING).....	63
FIGURE 33: A BLOCK 2 TEST STRUCTURE AND ITS FREE BODY DIAGRAM (IN-PLANE BENDING).....	65
FIGURE 34: A BLOCK 3 TEST STRUCTURE AND ITS FREE BODY DIAGRAM (AXIAL LOADING).....	72
FIGURE 35: A BLOCK 3 TEST STRUCTURE AND ITS FREE BODY DIAGRAM (IN-PLANE BENDING).....	74
FIGURE 36: SHOCK AMPLIFICATION FACTOR VS. SHOCK PARAMETER.....	81

Chapter 1: Introduction

Virtual qualification of microelectromechanical systems (MEMS) would be very advantageous and can tremendously aid in the design and development of new MEMS devices. To enable virtual qualification of MEMS devices that are subject to dynamic loading as in the case of navigation systems of gun launched artillery, it is essential to understand the changes to mechanical properties of the device material due to loading conditions. Specifically, knowing the dynamic strength of materials used would facilitate modeling and virtual qualification of new MEMS devices.

Single crystal silicon (SCSi), a brittle material, is a primary building block for many MEMS devices. Crystal plane orientation and surface flaws play a major role in influencing the fracture strength of silicon. Surface flaws, which are functions of processing techniques and device feature size, significantly influence the fracture strength of SCSi. Considerable research has been performed for identifying the quasi-static fracture strength of microfabricated silicon structures; however, there is a wide spread in the fracture strength data. Additionally, some research identifies the dynamic fracture strength of SCSi wafers with intrinsic flaws, but not that of microfabricated SCSi that accounts for the influence of processing techniques and device feature size on the fracture strength. Therefore, identification of dynamic fracture strength of microfabricated SCSi can play an important role in virtual qualification of new MEMS devices that are subject to dynamic loading.

Simple MEMS structures rather than functional MEMS devices should be employed in the experiments and analyses, because simplifying the geometry and loading will provide more confidence in the resulting strength measurements. After subjecting the test structures to a known shock load, the specimens should be inspected for structural failures. Once failure occurs, finite element analysis (FEA) should be used to identify the critical failure strength. Many different variants of this simple structure should be built by altering geometric and, potentially, processing details for performing a parametric study. Ideally, the parameter space investigated will encompass some structures that fail and some that survive and will make it easier to identify the failure strength envelope. A statistically significant number of experiments should be performed to fully understand the uncertainties in failure strengths, modes, and locations.

This thesis addresses the feasibility of assessing the influence of deep reactive ion etching (DRIE) technology on the dynamic fracture strength of SCSi at the University of Maryland (UMD). Chapter 2 reviews the existing information on fracture strength of SCSi. The development of test methodologies including identification of an appropriate dynamic testing method, preparation of test samples, subjection of test samples to dynamic loads, inspection of tested samples for structural failure, and identification of suitability of FEA for detection of the critical stress location and magnitude along with the natural frequencies is discussed in Chapter 3. Existing MEMS accelerometer dies provided by QinetiQ were used in the development of test methodologies described above. However, as discussed in Chapter 4, simple structures were eventually used in the feasibility study for evaluating the influence of DRIE technology on the dynamic fracture

strength of SCSi because the geometry of the actual accelerometer dies was too complex and no structural failures occurred for dynamic loadings up to 5000 g's. Chapter 5 summarizes the recommendations regarding test methodologies to be used in future work. In the near future, a statistically significant number of tests will take place to quantify the dynamic fracture strength of SCSi subjected to DRIE processing.

Chapter 2: Literature Review

Because SCSi is a main building block for many MEMS devices, the dynamic fracture strength of SCSi that was subjected to microfabrication processing is of interest for applications involving MEMS devices under dynamic loading conditions. A search of the literature revealed that considerable research has been performed to identify the quasi-static fracture strength of microfabricated silicon structures. However, a wide range in the fracture strength data was observed. In contrast, very few articles discussed the dynamic fracture strength of SCSi wafers with intrinsic flaws. This chapter summarizes the relevant research conducted to determine the fracture strength of SCSi. The ultimate goal is to compare these values to dynamic fracture strength measurements of DRIE-processed SCSi that will be performed at UMD in the near future.

A research group at the University of Heidelberg in Germany has subjected SCSi wafers with intrinsic flaws to dynamic loading using a nonlinear surface acoustic wave (SAW) technique [1] - [3]. The SCSi wafers did not include an artificial notch and were not subjected to microfabrication processing. The group investigated crack nucleation and propagation due to dynamic loading with SAW. A neodymium-doped yttrium aluminum garnet (Nd: YAG) laser was used to excite SAW pulses. The critical stress for crack initiation varied from ~ 1.6 GPa along the $[-1 \ -1 \ 2]$ direction in a (111) SCSi wafer to ~ 7 GPa along the $[1 \ -1 \ 1]$ direction in a (110) SCSi wafer. All of the wafers used were grown from a single crystal seed into a boule, diced, and then polished and were free from etching flaws. Therefore, the fracture strength values should be higher than

measurements on microfabricated SCSi structures fabricated along the same planes and directions.

Other researchers reported a material spall strength of ~ 1.4 GPa for SCSi wafers subjected to Nd: YAG laser ablation [4]. Laser ablation introduces shock loading to the SCSi wafers. SCSi (100) wafers having thicknesses from 250 to 675 microns were used in these experiments. Another research team determined the ideal tensile and shear strength of SCSi to be 22 GPa and 6.8 GPa, respectively [5]. The tensile strength is calculated for a stress oriented in a $\langle 111 \rangle$ direction, and the shear strength is calculated for a shear stress on the $\{111\}$ plane in a $\langle 112 \rangle$ direction.

A group at the United States Army Research Lab (ARL) at Aberdeen Proving Ground (APG) has evaluated the feasibility of incorporating commercial-off-the-shelf (COTS) MEMS devices into navigation systems for munitions [6] - [8]. MEMS devices such as accelerometers, gyroscopes, magnetic sensors, and pressure sensors were subjected to high acceleration environments using shock tables, air guns, and flight testing. These experiments provided only a pass/fail result that indicated some of the COTS MEMS devices can withstand accelerations ranging from 21,000 to 95,000 g's. The same group also performed a pass/fail test on a high-g accelerometer (ADXSTC3-HG) designed and fabricated by Analog Devices Inc. on a silicon on insulator (SOI) substrate with an epitaxial silicon device layer thickness of 10 microns [9] - [10]. The accelerometer was designed to measure in-plane acceleration of up to 10,000 g's in the presence of large cross-axis disturbances ($\pm 100,000$ g's). This type of accelerometer survived a 30,000

g's shock table experiment as well as a 15,000 g's flight launch. Unfortunately, no measurements of dynamic fracture strength were attempted in this research.

Researchers at MIT performed bi-axial quasi-static flexure tests on samples prepared from SCSi (100) wafers under five different conditions for identifying the fracture strength of the material [11]. The five conditions were: 1) mechanically polished (500 microns thickness), 2) mechanically polished (280 microns thickness), 3) chemically polished, 4) KOH-etched, and 5) DRIE-etched. The mechanically polished and the chemically polished wafers were tested as-received from the supplier and were not processed any further. KOH-etched wafers were etched in hot KOH solution (30% KOH by weight) at 85°C with an etch rate of 2 microns/minute. DRIE-etched wafers were etched using a Bosch DRIE process with an etch rate of 3 microns/minute. Wafers were cut into 10 mm × 10 mm square plate samples with a diamond dicing saw and were placed on a machined aluminum block containing a circular hole (7 mm diameter) for testing. The specimen was loaded using a 1.5 mm diameter steel ball bearing attached to a micro hardness indenter, and the force was measured by a 150 N capacity load cell. In this configuration, the surface of interest (bottom surface) was located on the opposite side from the loading point and subjected to in-plane bi-axial tensile bending stresses. All tests were performed in displacement control mode until failure, which occurred in ~30 seconds. Table 1 lists fracture strength and surface roughness values for bi-axial flexure samples with different surface conditions.

Table 1: Fracture strength values for bi-axial flexural samples [11].

Parameters	Mechanically polished	Mechanically polished	KOH-etched silicon	DRIE silicon	Chemically polished
Number of samples	19	30	25	20	10
Thickness (microns)	500	280	280	230	280
Roughness (microns)	~3	~1	~0.3	~0.3	~0.1
σ_0 (GPa)	1.2	2.3	3.4	4.6	>4

In addition, radiused hub flexure specimens were prepared from 400 microns thick SCSi (100) wafers with a Bosch DRIE process and subjected to quasi-static loading, similar to the bi-axial flexure tests, to produce an axisymmetric stress distribution with a stress concentration at the radiused transition between the vertical hub wall and the horizontal surface of the specimen [11]. Additionally, some of the radiused hub flexure specimens were isotropically etched with either a wet etchant (5% HF, 55% HNO₃, and 40% DI water) or SF₆ plasma for increasing the fracture strength. Table 2 lists fracture strength values for radiused hub flexure samples under different surface conditions.

Table 2: Fracture strength values for radiused hub flexural samples [11].

Parameters	DRIE silicon	DRIE + wet etch	DRIE + SF ₆ Dry etch
Number of samples	35	31	28
Polishing depth (microns)	NA	1.8	2.7
σ_0 (GPa)	1.51	2.9	4

The results demonstrated that DRIE process parameters influence etch performance, surface morphology and fracture strength of SCSi [12]. In order to identify the effects, the parameters were chosen systematically to create 50 sets of process conditions. The experiments indicated that anisotropy, etching uniformity, hub fillet radii, and surface roughness have strong dependence on chamber pressure, coil and electrode power, and reactant gases flow rate. Specimens with high surface roughness always exhibited low

fracture strength, but specimens with low surface roughness displayed a wide spread in fracture strength values. The experimental results indicated that additional factors such as critical flaw size also influence the fracture strength.

The effects of various etchants on the tensile strength of SCSi along $\langle 110 \rangle$ directions was investigated by a research group at the University of California at Los Angeles [13] – [15]. The etchants utilized were potassium hydroxide (KOH), ethylene diamine pyrochatechol (EDP), tetramethyl ammonium hydroxide (TMAH), and xenon difluoride (XeF_2). Average fracture strengths reported for KOH, EDP, TMAH, and XeF_2 etched SCSi were 0.66 GPa, 1.22 GPa, 0.85 GPa, and 1.01 GPa respectively. The results of this work indicate that fracture strength is sensitive to surface morphology, which in turn depends on etchant choice, etchant recipe, and mask alignment to crystal orientation (for KOH etching).

Another team studied the influence of specimen size on the bending strength of SCSi beams [16] – [17]. Nano-, micro-, and millimeter scale SCSi beams were fabricated on a (100) plane along $\langle 110 \rangle$ directions. The beams contained trapezoidal cross-sections because an aqueous solution of 20% TMAH, an anisotropic wet etchant, was used to etch the silicon. Table 3 lists the size scale, specimen label, dimensions, average bending strength, Weibull parameters, and number of samples for the SCSi test specimens. In addition, Figure 1 shows Weibull plots of the bending strength for SCSi beams of various size scales. As seen from the results, the average bending strength of SCSi ranged from 0.47 GPa for millimeter scale specimens to 17.53 GPa for nanometer scale specimens.

Table 3: Specimen dimensions, Weibull parameters, and bending strength for SCSi beams of various size scales [16] - [17]

Size Scale	Specimen Label	Upper Width (μm)	Lower Width (μm)	Thickness (μm)	Length (μm)	Avg. Bending Strength (GPa)	Scale Param. b (GPa)	Shape Param. m	# Samples
Nano	A	0.2	0.37	0.255	6	17.53	17.64	62.05	200
	B	0.3	0.47	0.255	6	15.26	15.42	26.62	52
	C	0.8	0.98	0.255	6	11.56	11.76	16.81	194
Micro	D	4.75	7.5	1.91	35	7.68	8.09	7.24	185
	E	48	74.5	19	360	3.70	4.14	4.20	229
Mili	F	1045	1800	520	9850	0.47	0.53	4.18	94

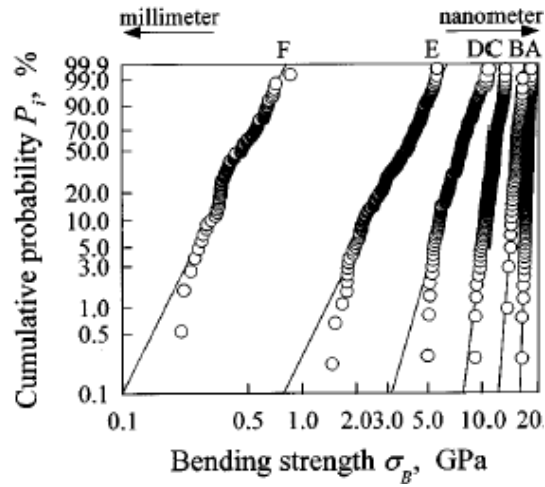


Figure 1: Weibull plots of bending strength for various size scale SCSi beams [16] - [17]

The quasi-static bending strength of chemo-mechanically polished SCSi wafers was studied [18]. SCSi wafers were placed concentrically on an aluminum platform with a hole at the center, and the load was applied with a ball bearing to produce an axisymmetric stress state. Bending strengths for (100) and (111) wafers were measured as $\sim 3\text{GPa}$ and 2.1GPa , respectively. In addition, mechanical damage from various lapping or grinding operations that penetrated deeper than $\sim 3\text{microns}$ significantly reduced the fracture strength to $0.3\text{-}0.4\text{GPa}$.

The ultimate strength of epitaxial silicon along $\langle 110 \rangle$ directions was investigated using micro-tensile bars and T-structures [19]. KOH etching was used to fabricate the test specimens. The average ultimate strength from micro-tensile bars was 1.21 GPa with a standard deviation of 0.35 GPa. However, the average ultimate strength from T-structures ranged from 0.555-0.951 GPa with a standard deviation of 0.047-0.108 GPa.

In summary, the fracture strength of SCSi wafers subjected to dynamic loading with SAW is of significant interest. Because the SCSi wafers did not include etching flaws, the results establish an upper bound on the expected dynamic fracture strength values of microfabricated SCSi. Additionally, the quasi-static fracture strength data of SCSi subjected to DRIE processing is important because the values can be compared to dynamic fracture strength measurements of DRIE processed SCSi that will take place at UMD. Next, the bending strength results of SCSi etched with TMAH show that the fracture strength values are greatly influenced by device feature sizes. Finally, the ARL-APG research subjected MEMS devices to dynamic loading conditions but only provided pass/fail results and no fracture strength measurements.

Chapter 3: Development of Test Methodologies

This chapter discusses the development of test methodologies that will be utilized to study the dynamic fracture strength of microfabricated SCSi structures at UMD. The process mainly consists of identification of an appropriate dynamic testing method, preparation of test samples, subjection of test samples to dynamic loads, inspection of tested samples for structural failure, and identification of suitability of FEA for detection of the critical stress location and magnitude as well as the natural frequencies. Existing MEMS dies provided by QinetiQ were used in the development of test methodologies.

Selection of Dynamic Testing Method

Many testing systems such as live guns, rail guns, air/gas guns, split Hopkinson pressure bars, and drop towers can be utilized for subjecting MEMS dies to dynamic loading.

Live gun testing is not a feasible design tool because it results in only a pass/fail type test, with no failure analysis possible on a “failed” test due to the extreme difficulty in recovering or soft catching the device after the gun launch. Additionally, live gun testing is very expensive and involves safety issues because it requires the use of cannon with live propellants [20]. Therefore, live gun testing is generally reserved for the last stage of design verification of gun launched systems.

Rail gun testing is a modified form of live gun testing where the projectile travels through a rail system, as shown in Figure 2. The rail system gradually descends and terminates in a trough of water, and the projectile employs a concave fitting on the end to slowly

decelerate in the water [20], [21]. Rail gun testing subjects the projectile to a high acceleration environment but also to a large amount of balloting. Additionally, rail gun testing is quite expensive.



Figure 2: A rail gun testing system [21]

Air guns use air pressure to propel projectiles and can generate accelerations of up to 15,000 g's, but the pulse duration is shorter than that of a live gun [21]. Figure 3 shows an example of an air gun system. Air gun testing is less expensive and is also safer than live gun testing since it does not involve live propellant. However, air gun testing requires an on-board recorder or a telemetry transmitter for collecting loading data, thus requiring a fairly complex data acquisition system. Gas guns are similar to air guns in regards to operation principle, safety, and cost except that gas guns use gas pressure to propel the projectiles. For the air and gas guns mentioned above, the projectiles experience acceleration pulses during the launch process. An alternate type of gun, which is used at ARL in Adelphi, slowly accelerates the projectile through the muzzle by air or gas pressure. After exiting the muzzle, the projectile enters a catch tube where it is decelerated with a honeycomb mitigator. Thus, the “acceleration” pulse is generated by the deceleration of the projectile [20]. The projectile is stationary after the test and requires no “soft catch”, which is very advantageous. However, this setup still requires an on-board recorder or a telemetry transmitter for collecting data.

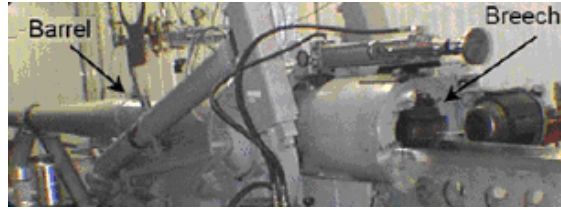


Figure 3: An air gun system [21]

A split Hopkinson pressure bar can provide strain rate on the order of $10^4/s$ [22]. Figure 4 shows a schematic of a split Hopkinson pressure bar system. The system is composed of 3 bars (striker, incident, and output), the test sample, a mechanism such as a gas gun for propelling the striker bar into the incident bar, and a momentum trap. When the striker bar impacts the incident bar, a stress wave travels through the length of the incident bar and reaches the test sample. Some of the energy gets transmitted through the test sample into the output bar and some is reflected back into the incident bar [20]. The bars have circular cross sections and are sized in a manner that allows the use of a one-dimensional approximation for the wave equation. MEMS dies are too small and fragile to be directly attached to a split Hopkinson pressure bar testing system. Additionally, the dies require a fixture that contains a flat surface for mounting, but a cylindrical specimen fixture is required to ensure one-dimensional wave propagation during the tests. Therefore, a split Hopkinson pressure bar would not be an appropriate dynamic testing method for the MEMS dies.

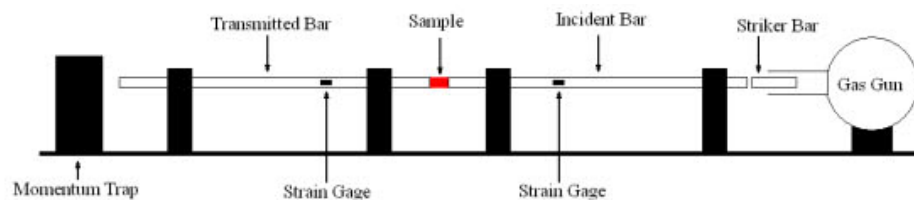


Figure 4: A split Hopkinson pressure bar schematic [22]

Drop tower testing is the most popular method of subjecting test samples to dynamic loading [20], [21]. A Lansmont system, which represents a typical drop tower design, is illustrated in Figure 5. Drop tower testing utilizes a raised platform for subjecting specimens to a high acceleration environment. During the test, the platform is released and falls either by gravity alone or with bungee cord assistance and subjects test specimens to an acceleration pulse that is generated from the deceleration of the drop table. The total energy (acceleration level) available from a drop tower system is limited by the drop height and elasticity of the bungee cords. The systems available for UMD research can easily achieve accelerations of up to 5,000 g's. Drop towers are easy to use, safe, and can provide much more reproducible results than the other types of dynamic loading systems. The main disadvantage of drop tower testing is the short duration (fractions of a millisecond) of the shock pulse. However, the pulse duration and shape can be modified by placing various materials such as elastomer pads, lead pellets, or pneumatic cylinders between the drop table and the base. For all of these reasons, drop tower systems were selected as the best dynamic loading system for testing MEMS dies for the UMD/QinetiQ project.



Figure 5: A Lansmont drop tower [23]

Description of Devices

QinetiQ provided the Center for Advanced Life Cycle Engineering (CALCE) at UMD with existing bare MEMS die structures minus the circuitry (50g accelerometers, 250g accelerometers, 1000g accelerometers, and 4g switches) to be used for developing the test methodologies. These MEMS dies were fabricated on SOI substrates with handle wafer thicknesses of 425 microns, device layer thicknesses of 100 microns, and buried oxide layer thicknesses of 3 microns. The silicon on both the device layer and the handle wafer is (100) p-type SCSi. The die fabrication process utilized photolithography, DRIE, and isotropic oxide etch techniques. The overall dimensions were 4.5×4.5 mm for the accelerometer dies and 4×4 mm for the 4g switch dies.

A detailed view of a 1000g accelerometer is shown in Figure 6 where white indicates an air gap, pink indicates a moving part, and blue indicates a fixed part. Silicon was under etched to release the moving parts. Square holes (9×9 microns) on the proof-mass and the moving fingers permit quicker release of the moving parts. The folded springs allow motion of the proof-mass and moving fingers when the accelerometer is subjected to acceleration. Mechanical stoppers constrain the proof-mass to move 2 microns along the axis of motion and prevent over-ranging of the accelerometers. Fixed and moving fingers are arranged like a comb drive with a sensing gap of 4 microns and a non-sensing gap of 28 microns. The fingers ($1000 \times 51 \times 100$ microns) form parallel plate capacitors into the page.

The 50g, 250g and 1000g accelerometers are identical in dimensions, except for the folded springs. The 1000g springs are the widest and the shortest, and therefore the stiffest. The 250g springs are as wide as the 1000g springs but longer. The 50g springs are the narrowest and the longest. Also, the 50g accelerometers have an additional set of mechanical stoppers. Figure 7 compares the 50g, 250g and 1000g spring geometries. Spring dimensions along with other dimensions for the accelerometers are provided in Appendix A. All information regarding the 4g switch is included in Appendix B since the switch was not subjected to extensive testing and modeling due to a tether that significantly restricted the motion of the switch.

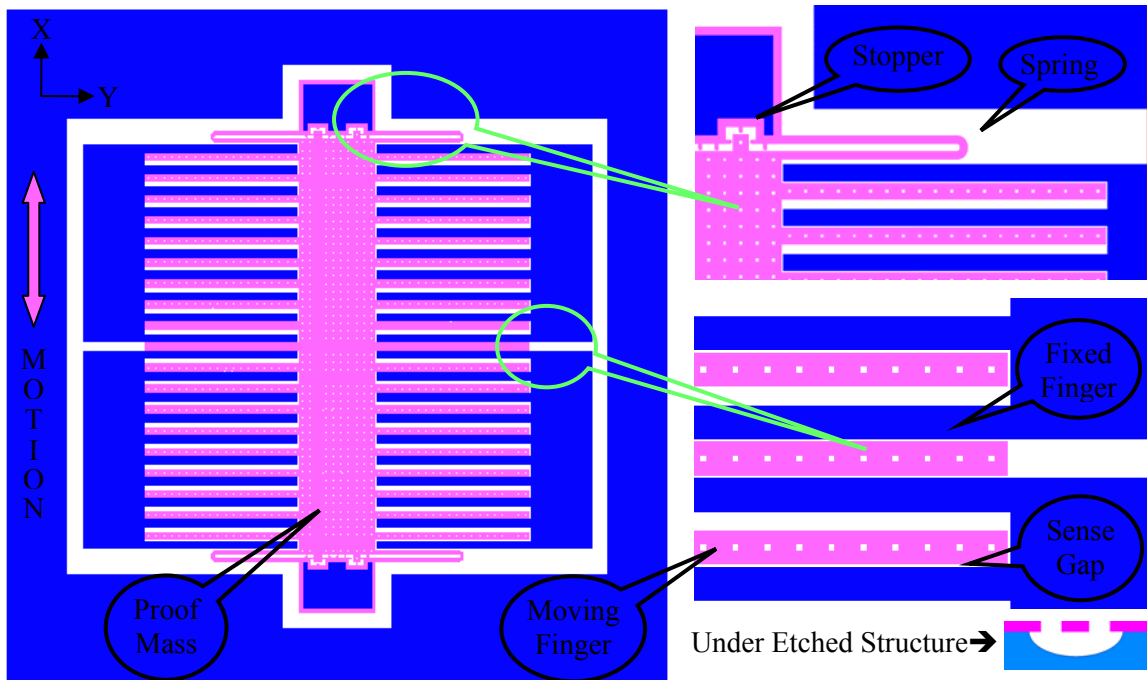


Figure 6: A detailed view of a 1000g accelerometer die layout

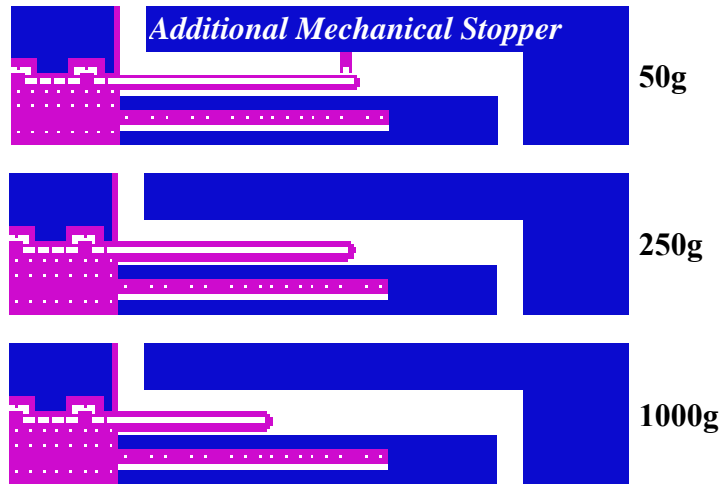


Figure 7: A comparison of 50g, 250g and 1000g spring geometries

Sample Preparation

A MEMS specimen fixture was used for attaching MEMS dies to the drop tower table. The specimen fixture had to be large enough to accommodate MEMS dies mounted along three orthogonal directions and for using a torque wrench to securely bolt the fixture to the drop table. However, the specimen fixture also had to be small enough to fit inside an environmental scanning electron microscope (ESEM) chamber for inspections. The specimen fixture, shown in Figure 8, is an aluminum block with dimensions of $32 \times 32 \times 15$ mm. Each fixture can accommodate MEMS dies on a maximum of three faces. MEMS dies on the bottom face of the fixture were mounted inside a pocket to prevent damage to the dies and to permit out-of-plane motion of the proof-masses.

Adhesive for attaching the MEMS dies to the specimen fixture had to be carefully selected to ensure that the dies remain attached to the fixture throughout the drop test and afterward. The adhesive bond must survive $>5,000$ g's during the drop tests. However, the adhesive was not required to be thermally or electrically conductive. Material data

sheets indicated that four EPO-TEK® brand adhesives (353ND, 930-4, H70E, and H65-175MP) would survive the dynamic loading [24]-[27]. However, three of the adhesives (930-4, H70E and H65-175MP) were also thermally conductive, which was not a required characteristic. Therefore, the remaining EPO-TEK® 353ND epoxy was selected to prepare drop test samples.

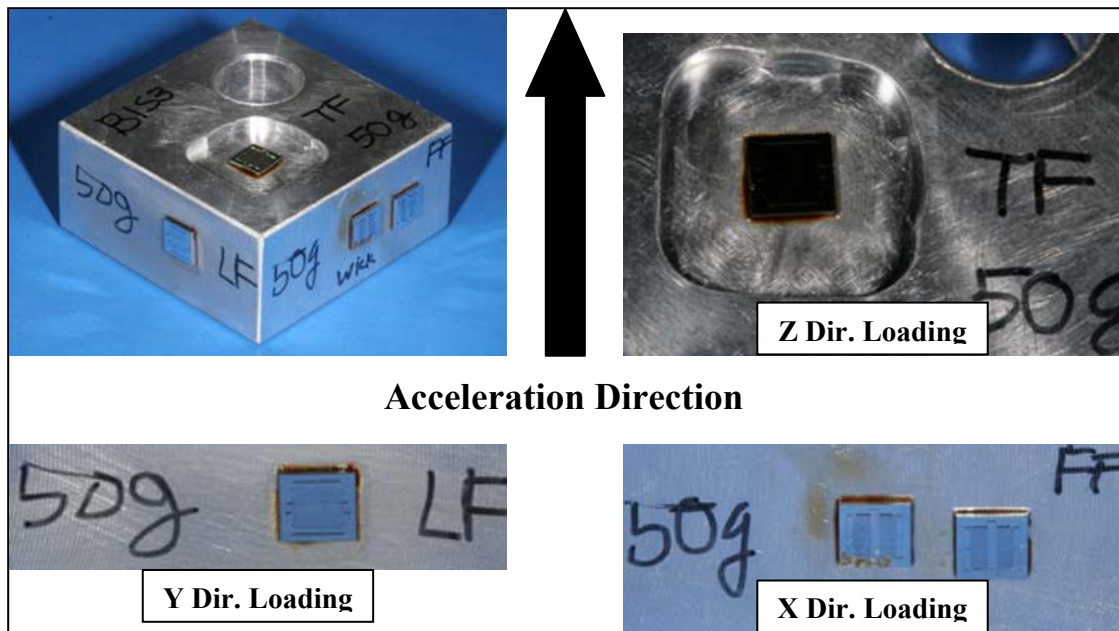


Figure 8: MEMS specimen fixture

High Acceleration Testing

MEMS dies were subjected to accelerations ranging from 1800 to 5000 g's along different directions with a drop tower. Figure 8 shows that accelerometers were oriented along three different axes to subject them to in-plane axial (x-direction), in-plane bending (y-direction), and out-of-plane bending (z-direction) accelerations. Table 4 provides a summary of the tests performed along with the device g rating, orientation of force along the device axis, number of drops completed at a corresponding g level, and the failure

results. Figure 9 provides the acceleration profiles from two of the drop tests performed, at 2000 g's and 5000 g's. It is observed that the acceleration pulse from a lower g test results in a cleaner profile than the higher g test. Also, the pulse duration is longer for a lower g experiment (0.5 ms for a 2000 g pulse versus 0.3 ms for a 5000 g pulse).

Table 4: Summary of Drop Tower Testing

Sample Label	Device g Level	Loading Direction (Device Axis of Motion = X)	# of Drops	Visible Failure
B1S1_LF	50	X	01 @ 1800g 10 @ 2000g 01 @ 4800g	No
B1S2_LF	50	X	01 @ 1800g 10 @ 2000g 01 @ 4800g	No
B1S3_FF	50	X	10 @ 2000g 01 @ 4800g	No
B1S3_LF	50	Y	10 @ 2000g 01 @ 4800g	No
B1S3_BF	50	Z	10 @ 2000g	No
B1S1_FF	250	X	01 @ 1800g 10 @ 2000g 01 @ 4800g	No
B1S2_FF	250	X	01 @ 1800g 10 @ 2000g 01 @ 4800g	No
B1S5_LF	1000	X	01 @ 4600g	No

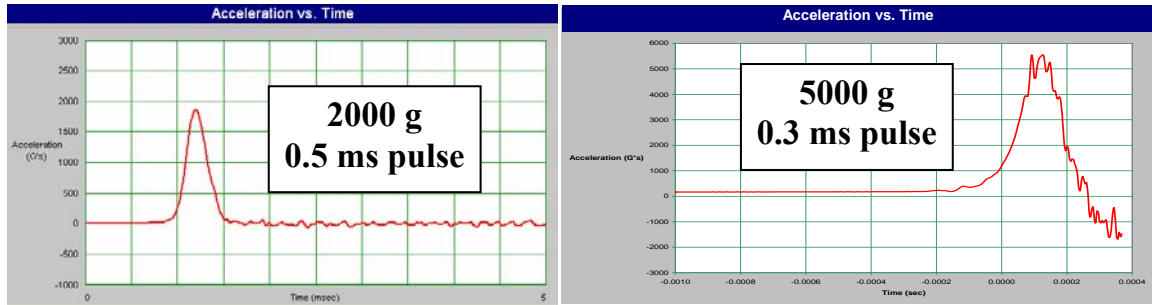


Figure 9: Acceleration profiles of drop tower tests

Structural Failure Inspection

Optical microscopy, ESEM, and X-Ray systems were considered as possible failure inspection methods initially. However, the X-Ray images of the MEMS dies were not clear because silicon and SOI do not provide good images when subjected to X-Ray inspection. An optical microscope was used for quick inspection of the MEMS dies. However, once the MEMS dies were mounted on the specimen fixture, an inverted optical microscope was needed for inspection since the fixture was too high to fit in an upright optical microscope. Using an inverted optical microscope was problematic due to the risk of damaging the MEMS dies during observations. Therefore, the ESEM is the preferred method for inspecting structures and surfaces due to its increased depth-of-field which offers better viewability. One problem encountered was that the sample often slid when the ESEM stage was tilted, but this effect was prevented by using double-sided tape to secure the sample inside the ESEM chamber. As seen from Table 4, the preliminary drop tests conducted did not result in any structural failures of the MEMS dies. Figure 10 shows before and after ESEM images of a 50g accelerometer subjected to a drop test at 1800 g's.

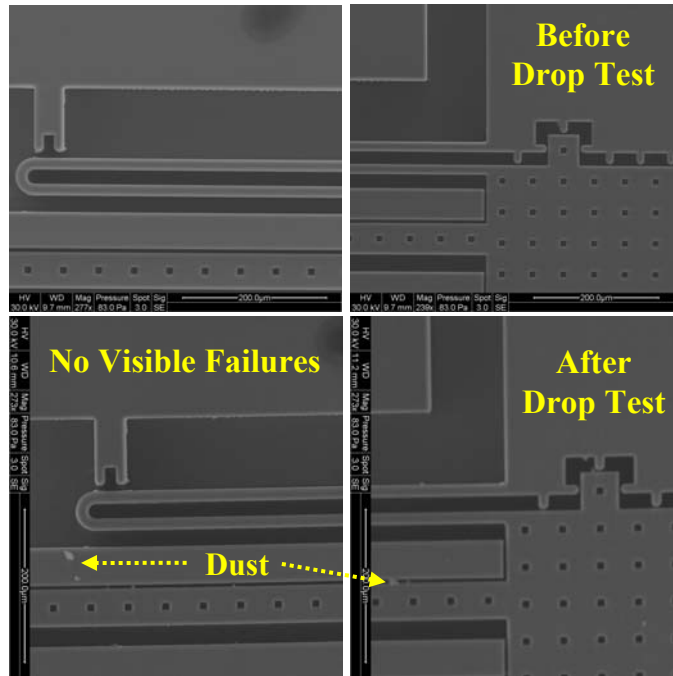
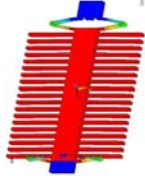
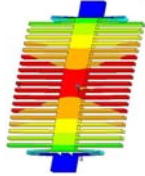
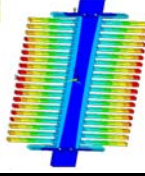
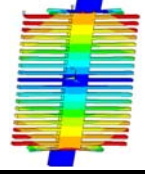


Figure 10: Before and after ESEM of a 50g accelerometer subjected to a 1800 g drop test

Finite Element Analyses and Shock Response

Modal analyses of the 50g, 250g and 1000g accelerometers were performed using ANSYS for identifying the natural frequencies and mode shapes of the dies. Table 5 lists the first four mode shapes and natural frequencies of the accelerometers. For the first mode, the accelerometers move in-plane in the x-direction. For the second mode, the accelerometers bow out-of-plane in the z-direction. For the third mode, the accelerometers rotate about the x-axis in the y-z plane. And for the fourth mode, the accelerometers twist about y-axis in the x-z plane. Rigid body motion of the proof-mass and the moving fingers was observed in the simulations. Also, modeling indicated that there would be no whipping or flexure of the fingers.

Table 5: Mode shapes and natural frequencies of 50g, 250g, and 1000g accelerometers

Mode Shape	Mode #	50g	250g	1000g
	1	2,457 Hz	5,147 Hz	9,686 Hz
	2	10,691 Hz	14,322 Hz	20,997 Hz
	3	14,413 Hz	18,554 Hz	23,430 Hz
	4	19,582 Hz	26,915 Hz	43,535 Hz

FEA of the accelerometer dies were performed using ANSYS for identifying the critical stress magnitudes and locations. Only a pair of symmetric moving fingers was used in the analyses to simplify the calculations, due to the rigid body motions of the moving fingers observed previously. The results of the finite element analyses indicated that the stresses are critical at the following three locations: spring & peninsula attach, spring & proof-mass attach, and proof-mass & moving finger attach. Critical stress locations for a 50g accelerometer are shown in Figure 11 (overall view) and Figure 12 (detailed view). Additionally, the computer analyses indicated that the critical stress values were only fractions of a GPa, which was too low to cause structural failures. Therefore, the FEA results validated the lack of failures observed in the experiments.

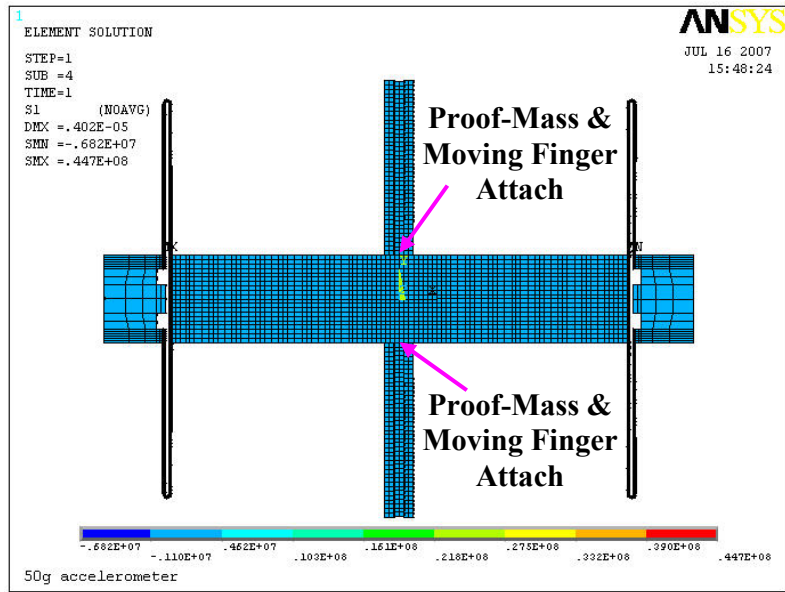


Figure 11: The first principal stress of a 50g accelerometer with a pair of moving fingers

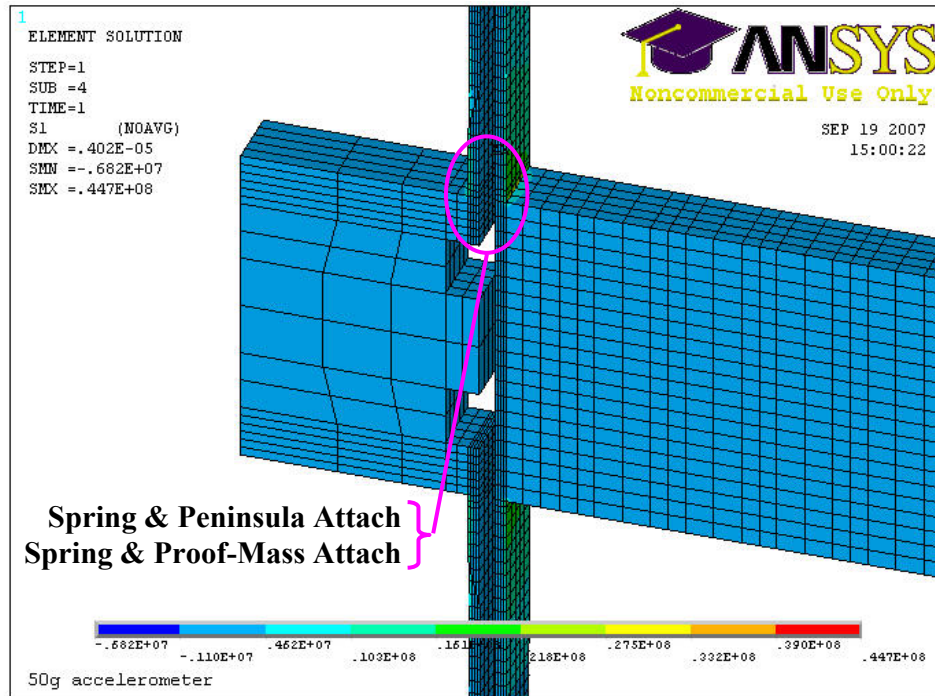


Figure 12: Detailed view of the first principal stress of a 50g accelerometer with a pair of moving fingers

In order to confirm whether the MEMS dies were excited during the drop tests, shock parameter ($f_n T$) values were calculated. Figure 13 shows that when the shock parameter value for a half sine wave is greater than ~ 0.45 , the dies are excited with an amplification factor of ≥ 1 . Table 6 provides shock parameter values, natural frequencies and pulse durations for 50g, 250g, and 1000g accelerometers when subjected to 2000g and 5000g drop tests. In all cases, the shock parameter values for the accelerometers are greater than 0.45; therefore, all the accelerometers were excited during the 2000g and 5000g drop tests.

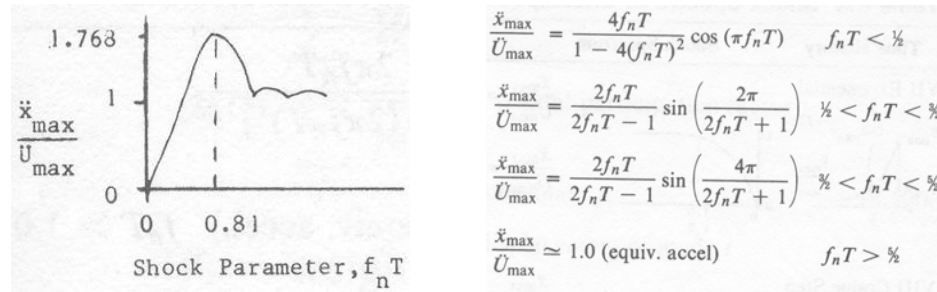


Figure 13: Shock response parameter relations [28]

Table 6: Shock parameter values of the 50g, 250g and 1000g accelerometers for 2000g and 5000g drop tests

Device g Level	Mode #	f_n (Hz)	T_{2000g} (s)	$f_n * T_{2000g}$	T_{5000g} (s)	$f_n * T_{5000g}$
50	1 – In Plane	2,457	5.0E-04	1.2	3.0E-04	0.7
	2 – Out of Plane	10,691	5.0E-04	5.3	3.0E-04	3.2
250	1 – In Plane	5,147	5.0E-04	2.6	3.0E-04	1.5
	2 – Out of Plane	14,322	5.0E-04	7.2	3.0E-04	4.3
1000	1 – In Plane	9,686	5.0E-04	4.8	3.0E-04	2.9
	2 – Out of Plane	20,997	5.0E-04	10.5	3.0E-04	6.3

Summary

Existing MEMS dies provided by QinetiQ were used in the development of test methodologies. The dies were mounted on the MEMS specimen fixtures along different orientations and subjected to drop tests with g levels ranging from 1800 to 5000 g's. After testing, specimens were inspected with an ESEM and no visible failures were observed. Subsequent FEA modeling indicated very low stress levels in the dies during the drop tests, thereby confirming that no failures should have occurred. During the failure inspections, some dust particles were observed on the MEMS dies because the test samples were not prepared in a cleanroom. To avoid future problems with dust particles, the next set of test samples should be prepared in a cleanroom. Logistics such as transporting the dies from England, including the required packaging and paperwork, and gaining access to dynamic testing facilities were established. While CALCE personnel verified the feasibility of conducting dynamic fracture strength tests of microfabricated SCSi structures at UMD, QinetiQ designed MEMS shock test structures that are expected to fail during the drop tests. Results on these new structures will be described in the following chapter.

Chapter 4: Application of Test Methodologies

In this chapter, the test methodologies that were developed previously are applied to the new proof-mass and cantilever beam shock test structures designed and manufactured by QinetiQ. New structures were adopted to simplify the configuration and loading, in order to easily identify the failure strength and provide more confidence in the test results.

Unlike the previous dies, these new MEMS shock test structures are supposed to reach critical stress levels and fail during the drop tests. The goal at this point is to cause structural failures of the new test structures and to identify a failure strength envelope for SCSi that was fabricated with DRIE processing. In the near future, a statistically significant number of tests will be performed by UMD personnel to fully characterize the uncertainties in the dynamic fracture strength values of SCSi subjected to DRIE processing.

Description of Devices

The MEMS shock test structures supplied by QinetiQ are categorized into three groups: Block 1, Block 2, and Block 3. The mask layout for these parametric structures is shown in Figure 14. Each type of block contains a different size proof-mass, which is uniform for all test structures on that block. However, the proof-masses are supported by cantilever beams of various lengths. Note that a (110) flat is located on one side of the wafer, to define the crystallographic planes and directions. As seen from the figure, all of the cantilever beams are oriented along $\langle 110 \rangle$ directions. A representative structure from each type of block, not to scale, is displayed in Figure 15.

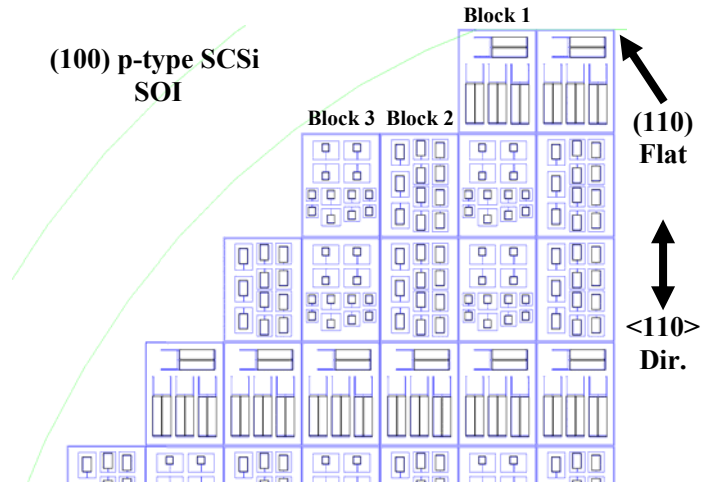


Figure 14: Mask layout of the MEMS shock test structures

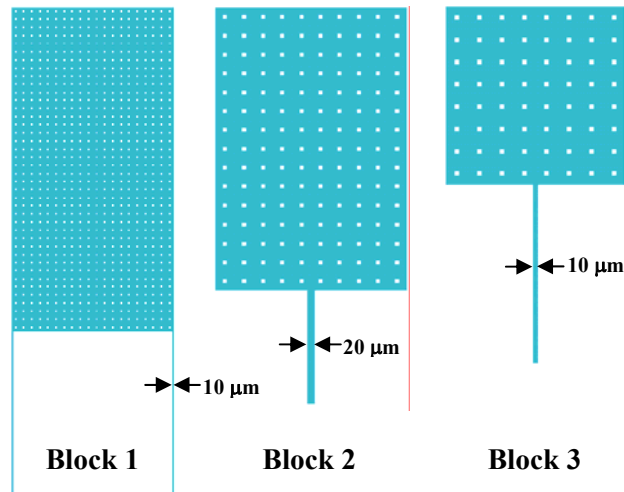


Figure 15: A representative shock test structure from each block type (not to scale)

Each of the Block 1 proof-masses ($2000 \times 1000 \times 100$ microns) is attached to two cantilever beams ($1000 \times 10 \times 100$ microns) as shown in Figure 15. Each Block 1 contains four parametric MEMS shock test structures with the same dimensions but with different gap widths (5, 10, 15, and 20 microns) between the cantilever beams and the side walls. However, the gap width between each proof-mass and the side walls in Block 1 is only 5 microns, which limits the in-plane bending motion.

Each of the Block 2 proof-masses ($750 \times 500 \times 100$ microns) is attached to a single cantilever beam as shown in Figure 15. The width and the depth of the Block 2 cantilever beams are 20 and 100 microns respectively. Block 2 contains three parametric MEMS shock test structures with cantilever beam lengths of 100, 200, and 300 microns. The gaps between the proof-masses and the side walls were 200 microns for the short (100 and 200 micron) beams and 250 microns for the long (300 micron) beams.

Each of the Block 3 proof-masses ($400 \times 400 \times 100$ microns) is attached to a single cantilever beam as shown in Figure 15. The width and the depth of the Block 3 cantilever beams are 10 and 100 microns respectively. Block 3 has four parametric MEMS shock test structures with cantilever beam lengths of 100, 200, 300, and 400 microns. The gaps between the proof-masses and the side walls were 150, 250, 350, and 550 microns for the 100, 200, 300, and 400 micron long beams, respectively.

Similar to the previous MEMS dies, the new shock test structures were fabricated on SOI substrates with a handle wafer thickness of 425 microns, a device layer thickness of 100 microns, and a buried oxide layer thickness of 3 microns. Also, the silicon on the SOI substrate is (100) p-type SCSi. QinetiQ fabricated these structures using the same process sequences (photolithography, DRIE, and isotropic oxide etching) as the previous dies. For faster release of the proof-mass from the handle substrate, 10×10 micron square holes are used to under etch the buried oxide layer.

Maximum Stress Determination

Since the MEMS shock test structures have simple geometries consisting of a proof-mass and one or two cantilever beams attached to a fixed wall support, it is relatively easy to analytically calculate the maximum stresses. The static stress values for shock test structures subjected to in-plane bending, out-of-plane bending, and axial loading under a 5000g acceleration pulse are calculated and tabulated in Appendix C. The critical loading direction is out-of-plane bending for Block 1 structures and in-plane bending for Block 2 and Block 3 structures. The worst-case dynamic stress values are estimated to be twice the static stress values because the dynamic response of an undamped single degree-of-freedom system subjected to a step acceleration pulse is double its static response [29]. Thus, an amplification factor of 2 was assumed for calculating the maximum dynamic stress values for the MEMS shock test structures subjected to 3000g and 5000g acceleration pulses along the critical loading directions, as listed in Table 7.

Table 7: Worst-case estimates of dynamic stress for shock test structures subjected to acceleration pulses (3000g and 5000g) along critical loading directions

Block	Cantilever Length (micron)	Max. Stress (GPa) 3000g Acceleration Pulse	Max. Stress (GPa) 5000g Acceleration Pulse
1	1000	1.58	2.63
2	100	0.35	0.59
	200	0.43	0.71
	300	0.50	0.83
3	100	0.38	0.63
	200	0.51	0.84
	300	0.63	1.05
	400	0.76	1.26

The maximum stress occurs at the wall support for all of the cantilever beams when subjected to bending loads. Figure 16 shows the maximum stress locations for Block 1,

Block 2, and Block 3 shock test structures. As highlighted in Table 7, the longest beams contain the highest stresses. Therefore, the structures with the longest cantilever beams within each block type are expected to fail first near the wall supports.

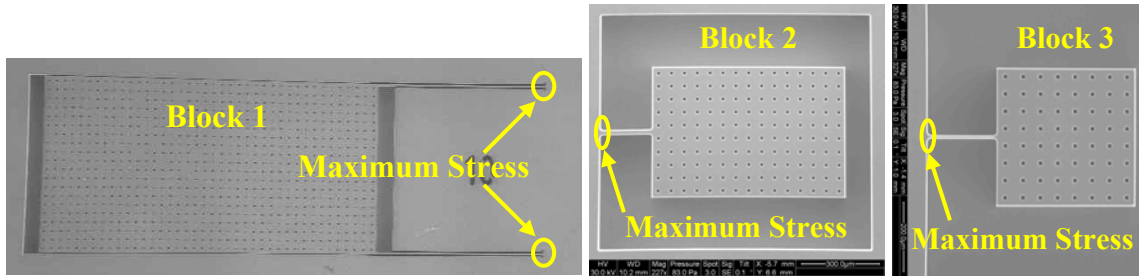


Figure 16: Maximum stress locations for Block 1, Block 2, and Block 3 structures

Dynamic Testing Methodology

The MEMS dies were mounted on specimen fixtures and subjected to acceleration pulses along the critical loading directions using a drop tower in an attempt to cause structural failures of the shock test structures. Figure 17 shows a MEMS specimen fixture that contains two dies mounted on the side. Occasionally the dies would rotate slightly during the epoxy curing process; however, orientation errors were not significant because the cosine of small angles is ~ 1 . Two drop towers with different drop table sizes were used for the dynamic testing. The MEMS dies were subjected to 3000g acceleration pulses with the small drop table (Lansmont Shock Tester) and 5000g acceleration pulses with the large drop table (IMPAC 66 Vertical Shock Machine). Figure 18 shows the acceleration profiles of a 3000g and a 5000g drop test. As expected, the drop tower with the smaller drop table produces a cleaner pulse. Table 8 provides a summary of the tests performed along with the block label, loading direction, number of drops performed at a corresponding g level, and the failure results.

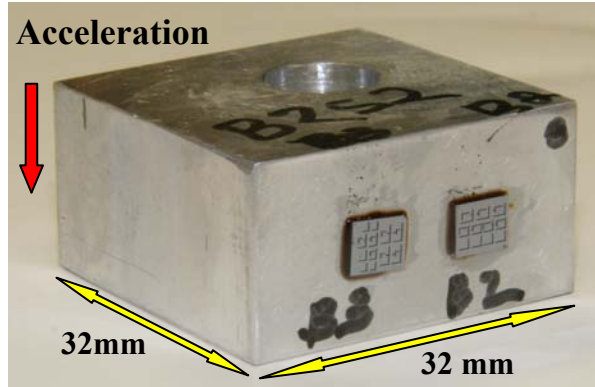


Figure 17: A MEMS specimen fixture with two dies (a Block 2 and a Block 3) mounted on the side for subjecting the shock test structures to in-plane bending motion

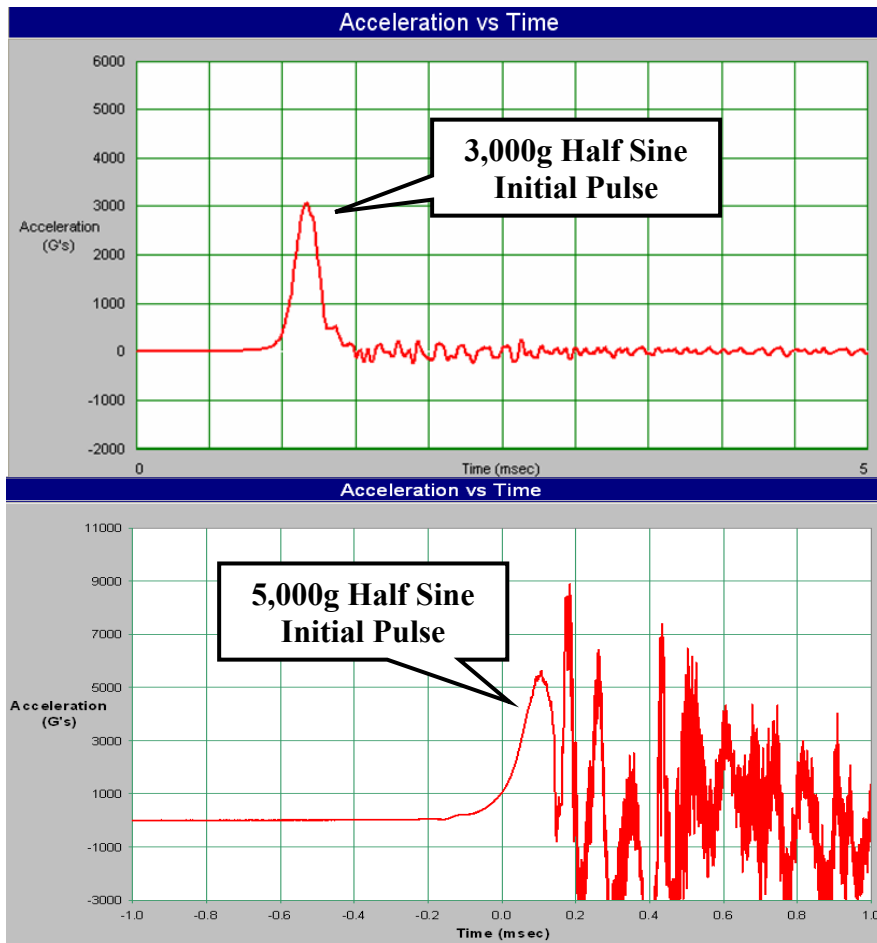


Figure 18: Acceleration profiles of a 3000g drop test (top) and a 5000g drop test (bottom)

Table 8: Drop tower testing summary

Sample Label	Block Label	Loading Direction	# of Drops @ g Level	Visible Failure
B2S1	Block 1	In-Plane Bending & Axial Loading	2 @ 5,000g	No
	Block 2	In-Plane Bending	2 @ 5,000g	Yes
B2S2	Block 2	In-Plane Bending	1 @ 5,000g	Yes
	Block 3	In-Plane Bending	1 @ 5,000g	Yes
B2S3	Block 2	In-Plane Bending	1 @ 5,000g	Yes
	Block 3	In-Plane Bending	1 @ 5,000g	Yes
B2S4	Block 2	In-Plane Bending	1 @ 5,000g	Yes
	Block 3	In-Plane Bending	1 @ 5,000g	Yes
B2S5	Block 2	In-Plane Bending	1 @ 3,000g	No
	Block 3	In-Plane Bending	1 @ 3,000g	No
B2S6	Block 1	Out-of-Plane Bending	1 @ 3,000g	Yes

Testing Results

Within each block type, the structures with the longest cantilever beams were expected to fail first near the wall support, which corresponds to the location of the highest stresses. However, when the Block 2 and the Block 3 dies were subjected to 5000g acceleration pulses along the critical loading direction, the shortest cantilever beams within each block type failed instead. Figure 19 shows that all of the 100 micron long cantilever beams failed in the Block 2 and Block 3 dies. In addition, Figure 19 also indicates that one of the 200 micron long cantilever beams failed in Block 3. These results were unexpected. Table 9 summarizes the structural failures of Block 2 and Block 3 shock tests structures that were subjected to 5000g acceleration pulses with the larger drop table. For both blocks, most of the failures occurred in the shorter beams and not a single failure was observed among the longest cantilevers. One possibility is that the proof-masses attached to the longer cantilevers were hitting the side walls, thus preventing maximum stress

levels from being reached. By multiplying the maximum static deflections from Appendix C with a factor of 2, the worst-case estimate of dynamic deflections were calculated as 105 and 251 microns for the longest Block 2 and Block 3 structures, respectively. Both of these values are much smaller than the corresponding gap distances of 250 and 550 microns, which clearly shows that the proof-masses were not impacting the side walls.

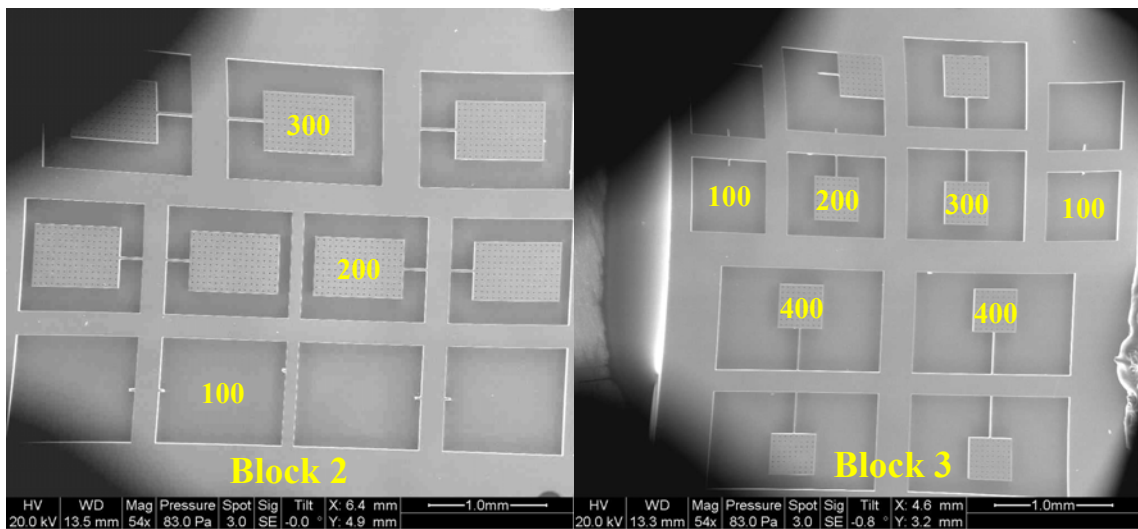


Figure 19: ESEM images of a Block 2 die (left) and a Block 3 die (right) that were subjected to a 5000g acceleration pulse with an IMPAC 66 Vertical Shock Machine

Table 9: Failure summary of Block 2 and Block 3 shock test structures subjected to 5000g drop tests

Block	Cantilever Length (μm)	# Tested	# Failed	% Failure
2	100	20	14	70.00%
	200	20	0	0.00%
	300	12	0	0.00%
3	100	10	10	100.00%
	200	5	1	20.00%
	300	6	2	33.33%
	400	9	0	0.00%

During inspection (before and after testing) of the dies with ESEM, etching anomalies were found in the MEMS shock test structures as shown in Figure 20 and Figure 21. Figure 20 illustrates streak mark etching anomalies near the bottom surface of the cantilever beams, and Figure 21 displays wavy surface etching anomalies on the side of the cantilever beams. Although both types of anomalies were observed, the streak mark etching anomalies were more prevalent in the shock test structures. Figure 21 and Figure 22 show failures of the test structures that were subjected to in-plane bending. Both figures indicate that the failures occurred along $\{111\}$ planes and originated at or near etching anomalies. This result was not surprising because SCSi is arranged in a diamond cubic (DC) crystal structure, which is a special form of a face-centered cubic (FCC) structure [30]. It is well known that materials containing FCC and DC structures fail on $\{111\}$ planes, which are the weakest [1], [30]. Note that the ESEM photographs were taken from oblique directions to better illustrate the fracture planes, so the angles will appear distorted. In addition, the cantilever beam failures appeared to begin at one of the side surfaces, as would be expected from in-plane bending loads.

Etching anomalies were present on all of the MEMS dies and were always located near the eventual fracture planes. These anomalies produced rough areas that acted as stress concentrations on an otherwise smooth surface. Since SCSi is a brittle material, it is likely that small flaws or cracks developed in these regions of high stresses and served as initiation points for the failures. Unfortunately, the flaws are not readily visible in the ESEM images because much higher magnifications are required.

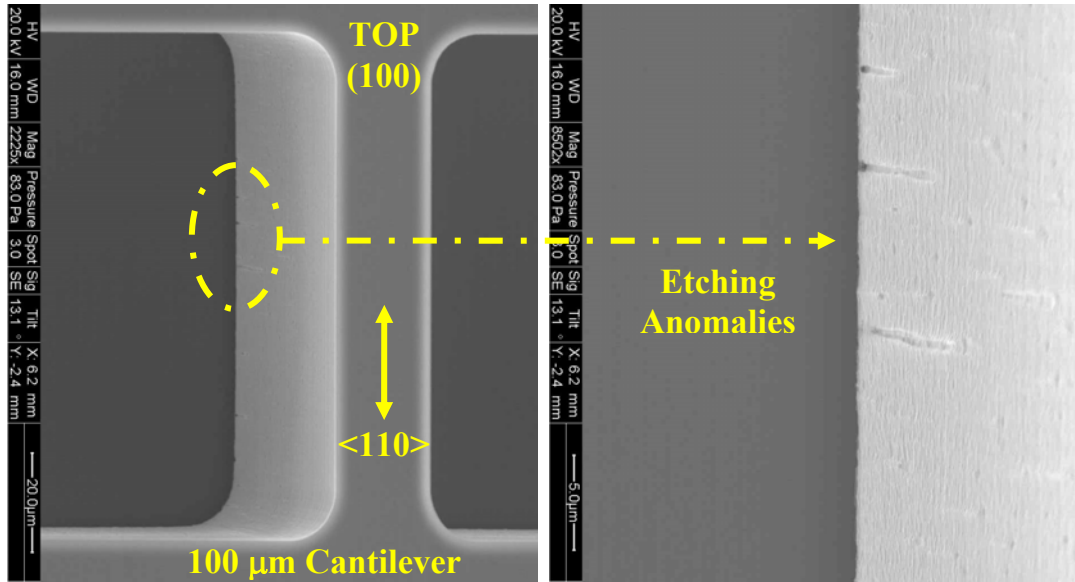


Figure 20: ESEM images of streak mark etching anomalies found in the shock test structures

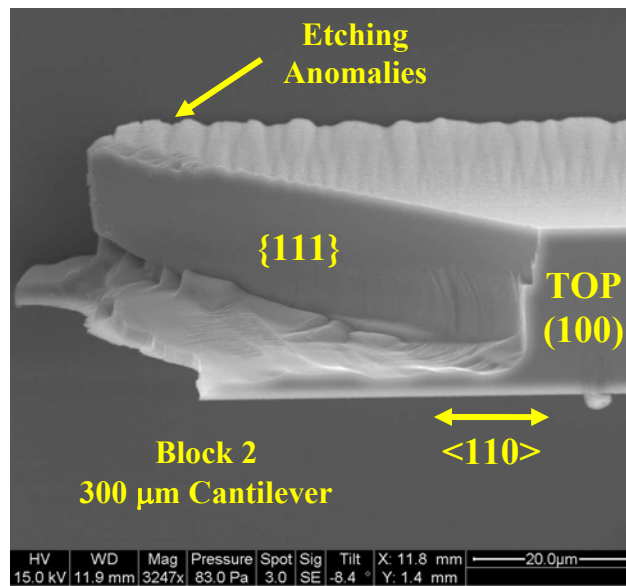


Figure 21: An ESEM image of wavy etching anomalies found in the shock test structures

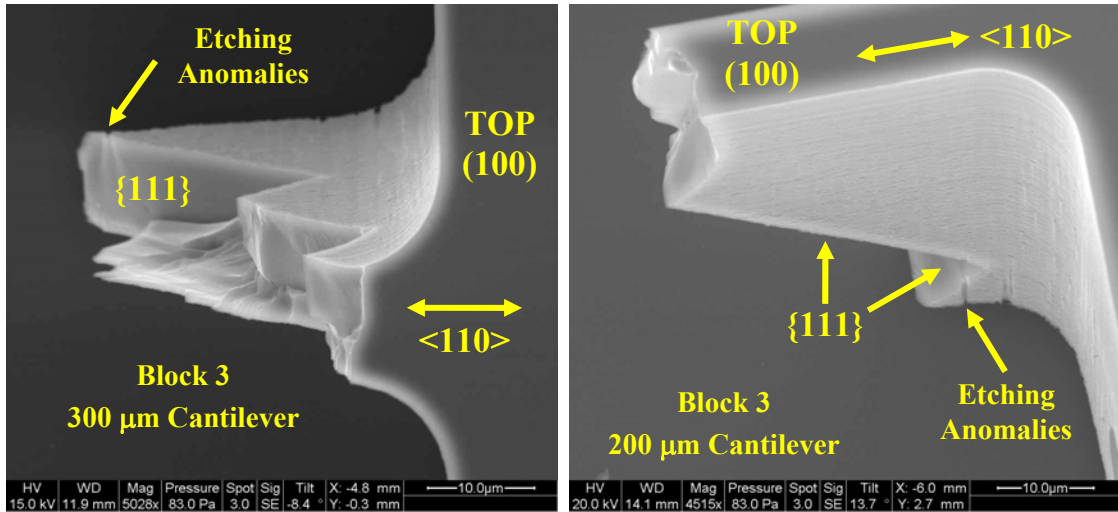


Figure 22: ESEM images of structural failures of MEMS shock test structures

When Block 1, Block 2, and Block 3 dies were subjected to a 3000g acceleration pulse along the critical loading direction using the smaller drop table, only the Block 1 structures failed. Figure 23 shows that all the Block 1 structures and none of the Block 3 structures failed during this test. Figure 24 illustrates that the Block 1 structures failed near the wall support and that the failure propagated from the bottom surface of the beam to the top surface of the beam, as would be expected for out-of-plane bending. Figure 24 also indicates that failures again occurred along {111} planes.

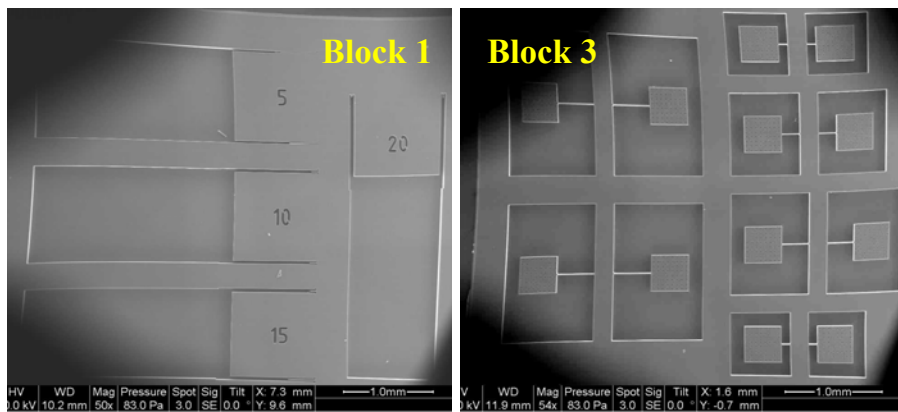


Figure 23: ESEM images of a Block 1 die (left) and a Block 3 die (right) that were subjected to a 3000g acceleration pulse with a Lansmont Shock Tester

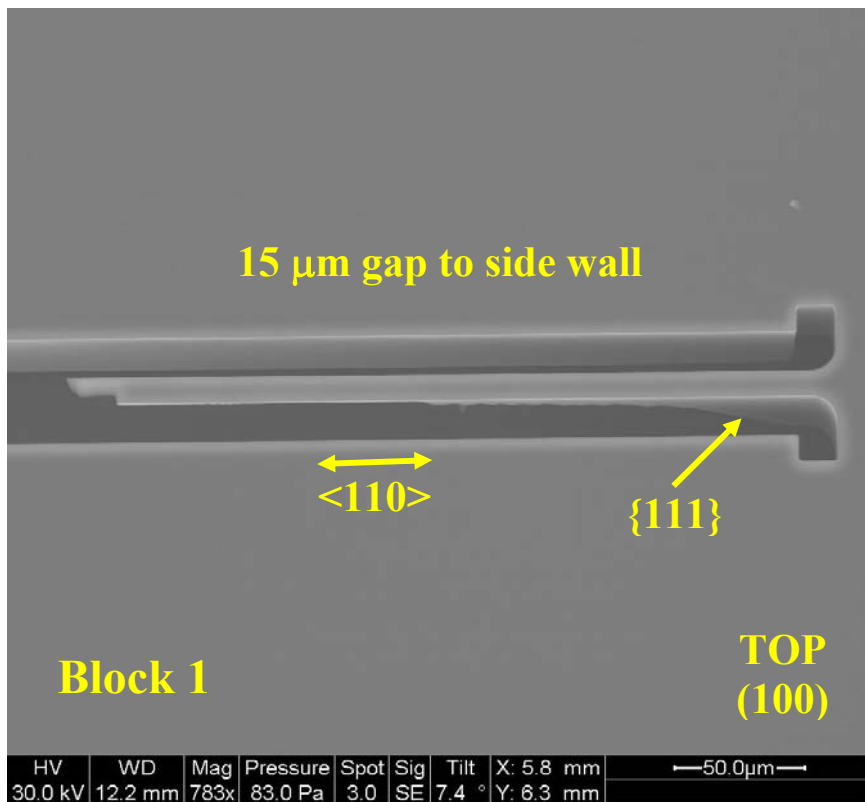
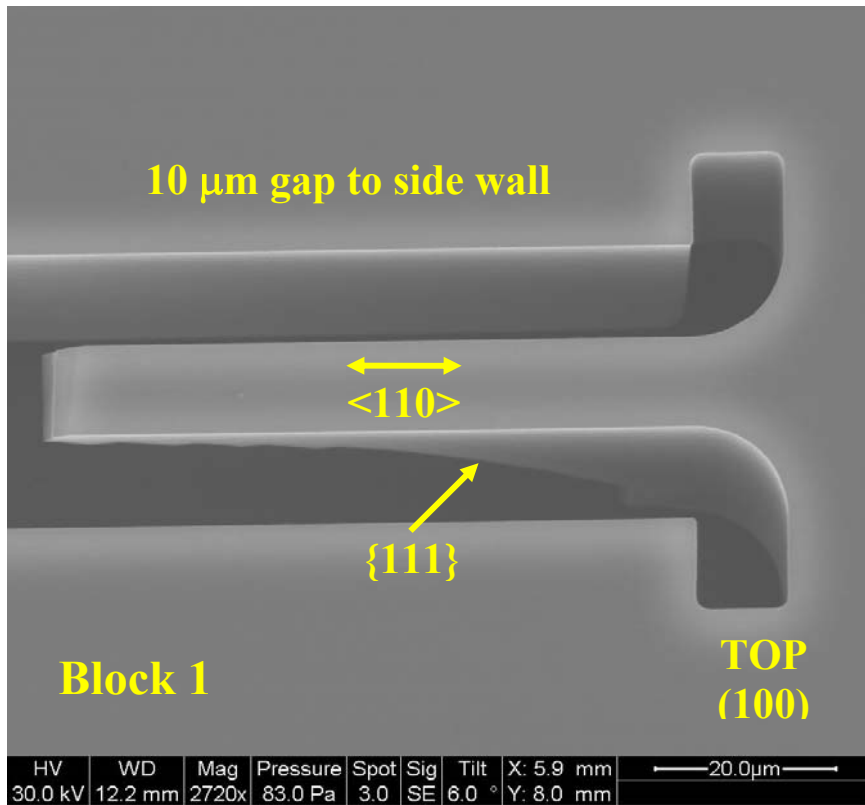


Figure 24: ESEM images of structural failures of Block 1 shock test structures

Discussion

Modal analyses of the Block 2 and Block 3 shock test structures were performed using ANSYS to investigate whether resonance was the possible cause for the unexpected failures of the 100-micron cantilever beams. The first natural frequencies for each cantilever beam length of Block 2 and Block 3 test structures are listed in Table 10. As expected, the natural frequencies decrease as the cantilever beam lengths increase for each block type. The first natural frequencies for 100-micron cantilever beam structures from Block 2 and Block 3 are 11.32 kHz and 10.39 KHz respectively. Figure 25 shows the complete time history plot of a 5000g drop test that was performed on the larger drop table. Note that this is an extended version of the shock profile from Figure 18, which only shows the initial peak of the pulse. The shape of the time history plot in Figure 25 suggests that the structures experienced high-amplitude and high-frequency vibrations for several milliseconds after the initial loading. In order to determine the frequency content of the acceleration pulse, a fast Fourier transform (FFT) of the time history plot was performed. The resulting FFT of the pulse is illustrated in Figure 26 and indicates peak frequency content at 9.57 kHz, 10.64 kHz, and 12.34 kHz. These frequencies are relatively close to the first natural frequencies of the 100-micron cantilever beam structures. Therefore, resonance due to high frequencies present in the acceleration pulse is believed to be the reason for failure of the shorter cantilever beams, whereas the longer cantilever beams with higher calculated stresses did not fail.

Table 10: The first natural frequency of Block 2 and Block 3 structures

Block	Cantilever Length (μm)	Natural Frequency (Hz)
2	100	11,318
	200	7,406
	300	5,578
3	100	10,387
	200	6,369
	300	4,550
	400	3,486

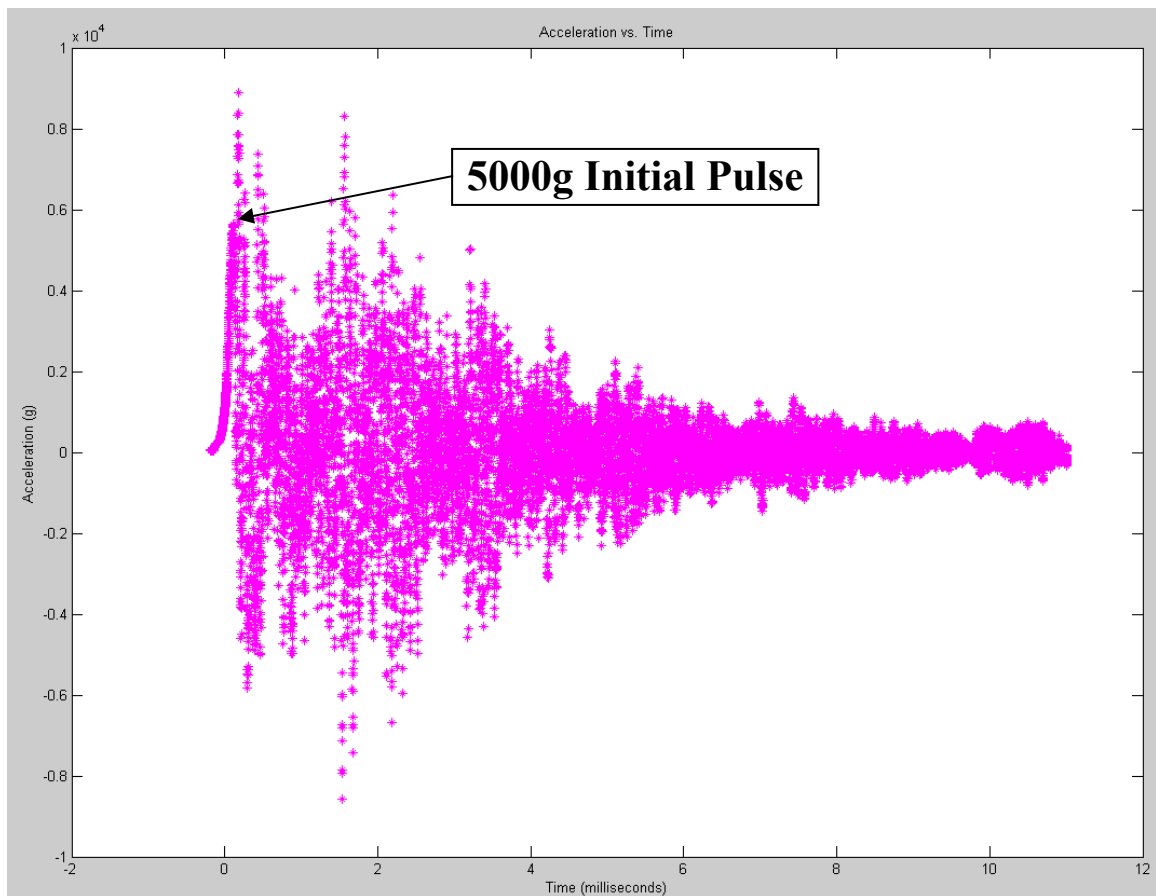


Figure 25: Complete time history plot of a 5000g drop test

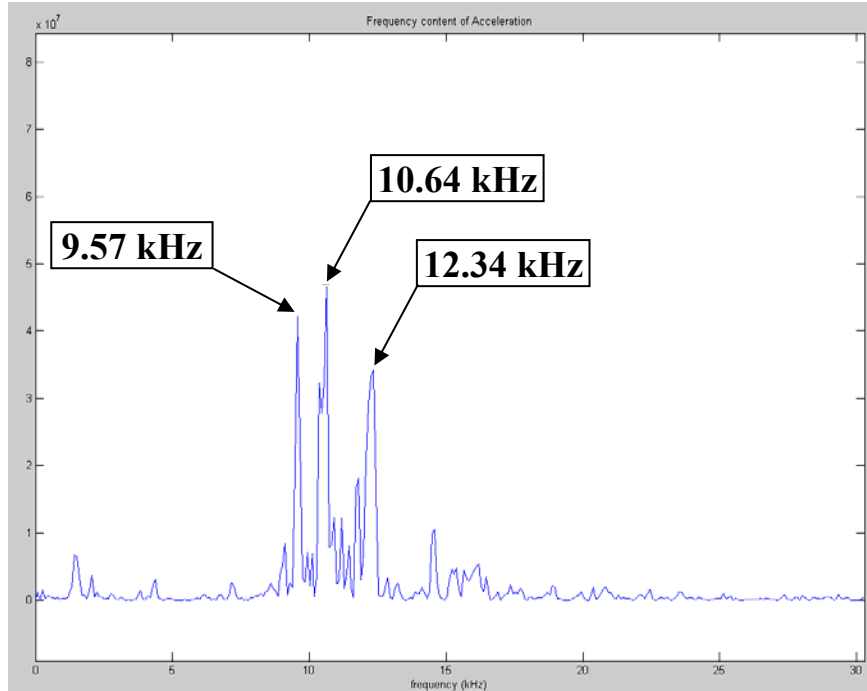


Figure 26: FFT of time history plot showing peaks at 9.57 kHz, 10.64 kHz, and 12.34 kHz

Shock parameter ($f_n T$) values were calculated to verify whether Block 1, Block 2, and Block 3 shock test structures were excited during the drop tests. As mentioned previously, shock test structures are excited with an amplification factor of ≥ 1 when the shock parameter value for a half sine wave is greater than ~ 0.45 [28]. Table 11 provides shock parameter values, natural frequencies, and pulse durations for the MEMS shock test structures when subjected to 3000g and 5000g acceleration pulses, such as shown in Figure 18. From that figure, the initial acceleration pulse for both the 3000g and the 5000g drop tests appears to be a half-sine pulse. In all cases, the shock parameter values for the test structures are greater than 0.45; therefore, all of the shock test structures were excited during the 3000g and 5000g drop tests.

Table 11: Shock parameter of Block 1, Block 2, and Block 3 structures

Block	Length (μm)	f_n (Hz)	T_{3000g} (s)	$f_n * T_{3000g}$	T_{5000g} (s)	$f_n * T_{5000g}$
1	1000	2,378	4.1E-04	0.97	2.8E-04	0.67
2	100	11,318	4.1E-04	4.64	2.8E-04	3.17
	200	7,406	4.1E-04	3.04	2.8E-04	2.07
	300	5,578	4.1E-04	2.29	2.8E-04	1.56
3	100	10,387	4.1E-04	4.26	2.8E-04	2.91
	200	6,369	4.1E-04	2.61	2.8E-04	1.78
	300	4,550	4.1E-04	1.87	2.8E-04	1.27
	400	3,486	4.1E-04	1.43	2.8E-04	0.98

Previously, an amplification factor of 2 was used to estimate the worst-case dynamic stress values. However, the true shock amplification factors for half-sine pulses can be calculated from the shock parameter relations as described in Appendix D. Shock amplification factors and the actual dynamic stress values for the MEMS shock test structures subjected to 3000g and 5000g drop tests are listed in Table 12.

Table 12: Shock amplification factors and actual dynamic stress values for shock test structures subjected to 3000g and 5000g drop tests

Block	Cantilever Length (μm)	3000g Shock Parameter	3000g Shock Amp. Factor	3000g Dynamic Stress (GPa)	5000g Shock Parameter	5000g Shock Amp. Factor	5000g Dynamic Stress (GPa)
1	1000	0.97	1.74	1.37	0.67	1.74	2.29
2	100	4.64	1.00	0.18	3.17	1.00	0.29
	200	3.04	1.00	0.21	2.07	1.24	0.44
	300	2.29	1.15	0.29	1.56	1.47	0.61
3	100	4.26	1.00	0.19	2.91	1.00	0.32
	200	2.61	1.00	0.25	1.78	1.36	0.57
	300	1.87	1.32	0.42	1.27	1.62	0.85
	400	1.43	1.54	0.58	0.98	1.74	1.10

The calculated maximum stress is 1.37 GPa for Block 1 test structures subjected to out-of-plane bending around $\langle 110 \rangle$ directions with a 3000g acceleration pulse. Since all of the shock test structures failed when Block 1 was subjected to a 3000g acceleration pulse, the dynamic strength of (100) SCSi must be less than 1.37 GPa for these test conditions.

The calculated maximum stress is 1.10 GPa for Block 3 test structures with cantilever beam lengths of 400 microns subjected to in-plane bending around $\langle 100 \rangle$ directions with a 5000g acceleration pulse. Since the 400 micron cantilever beam structures were excited (shock parameter is 0.98, which is > 0.45 threshold) when Block 3 experienced a 5000g acceleration pulse and none of the 400 micron cantilever beam structures failed, the dynamic strength of (100) SCSi must be greater than 1.10 GPa in this case. Therefore, experimental results so far suggest that the dynamic fracture strength of DRIE processed (100) SCSi is greater than 1.10 GPa for bending around $\langle 100 \rangle$ directions and less than 1.37 GPa for bending around $\langle 110 \rangle$ directions. However, a statistically significant number of tests must still be performed to refine the dynamic fracture strength predictions and to quantify the uncertainties in the strength measurements. The smaller drop table should be used in all future experiments to avoid resonance failures due to high frequencies present in the acceleration pulses. Repeatable failures from cleaner pulses can be used in ANSYS-LSDYNA modeling to identify the failure strength of the material.

Chapter 5: Conclusion

SCSi is a main building block for many MEMS devices. Therefore, identification of the dynamic fracture strength of SCSi can tremendously aid in virtual qualification of new MEMS devices that are subject to dynamic loading. But since silicon is a brittle material, crystal plane orientation and surface flaws play a major role in influencing the fracture strength. Surface flaws, which are functions of processing techniques and device feature size, significantly influence the fracture strength of SCSi. Some research identifies the dynamic fracture strength of SCSi wafers with intrinsic flaws, but not that of microfabricated SCSi that accounts for the influence of processing techniques and device feature size on the fracture strength. Therefore, identification of dynamic fracture strength of microfabricated SCSi can play an important role in virtual qualification of new MEMS devices that are subject to dynamic loading. In order to maximize the chance of success in the identification of dynamic fracture strength of microfabricated SCSi, it is advisable that the effect of a process technique such as DRIE on the dynamic fracture strength should be considered first. This thesis addressed the feasibility of assessing the influence of DRIE technology on the dynamic fracture strength of SCSi at UMD.

In order to evaluate the feasibility of assessing the influence of DRIE on the dynamic fracture strength of SCSi at UMD, a set of methodologies had to be developed and tested out. Existing bare MEMS accelerometer dies minus the circuitry were provided by QinetiQ to be used in the development of test methodologies. Drop tower testing was selected as the method for subjecting MEMS dies to dynamic loading because it is very

inexpensive, easy to use, safe, and can provide reproducible results. Bare MEMS accelerometer dies were mounted on aluminum drop tower MEMS specimen fixtures along different orientations with EPO-TEK® ND353 epoxy and were subjected to drop tests with g levels ranging from 1800 to 5000 g's. ESEM was used to inspect tested samples for failure rather than optical microscopy due to the increased depth of field which offered better viewability. Inspection of the drop tested samples revealed no visible failure. FEA modeling of the dies confirmed that no failures should have occurred from the drop tests using a preliminary estimate of the dynamic fracture strength. The shock parameter values for the accelerometers indicated that all the accelerometers were excited when subjected to drop tests ranging from 1800 to 5000 g's. There were some dust particles on the MEMS dies because the test samples were not prepared in a cleanroom, but it was felt that the dust did not affect the outcome. Logistic issues such as transportation and packaging of the fabricated dies as well as access to dynamic testing facilities were worked out.

While CALCE personnel worked on developing test methodologies for evaluating the influence of DRIE on the dynamic fracture strength of SCSi, QinetiQ designed and fabricated DRIE SCSi MEMS shock test structures for use in dynamic fracture strength experiments. These MEMS structures were specifically designed to reach critical stress levels with drop tests. The test methodologies previously developed were applied to these samples. Expected maximum stresses for the various parametric structures were easily calculated analytically due to the simple proof-mass and cantilever beam geometry. The worst-case dynamic stress values were estimated to be twice the static stress values

because the dynamic response of an undamped single degree-of-freedom system subject to step acceleration is double its static response [29]. After the drop tests were performed, however, the true shock amplification factors were calculated from the shock parameter relations to identify the actual dynamic stresses experienced by the shock structures during the 3000g and 5000g drop tests.

The MEMS shock test structures were mounted on MEMS specimen fixtures and were subjected to 3000g (small drop table) and 5000g (large drop table) acceleration pulses along critical loading directions. Resonance due to the high frequency content of the acceleration pulse from the larger drop table was identified to be the cause of unexpected failures of 100-micron long cantilever beam structures. Based on the analytical stress calculations and experiments performed thus far, the dynamic fracture strength of DRIE processed (100) SCSi is identified to be greater than 1.10 GPa for bending around $\langle 100 \rangle$ directions and less than 1.37 GPa for bending around $\langle 110 \rangle$ directions. A statistically significant number of experiments will be performed in the imminent future to identify the dynamic fracture strength and the uncertainties in the strength value of SCSi subjected to DRIE processing.

This thesis discussed the feasibility of assessing the influence of DRIE on the dynamic fracture strength of SCSi at UMD and developed a methodology for performing a statistically significant number of experiments. It has been established that failures of the shock test structures can be caused by the testing facilities available to/at UMD and that failure starts at/near the surface anomalies generated by the etching process.

Additionally, based on the analytical stress calculations and experiments performed up to this point, the dynamic fracture strength of DRIE processed (100) SCSi is greater than 1.10 GPa for bending around $\langle 100 \rangle$ directions and less than 1.37 GPa for bending around $\langle 110 \rangle$ directions.

Recommendations for Future Work

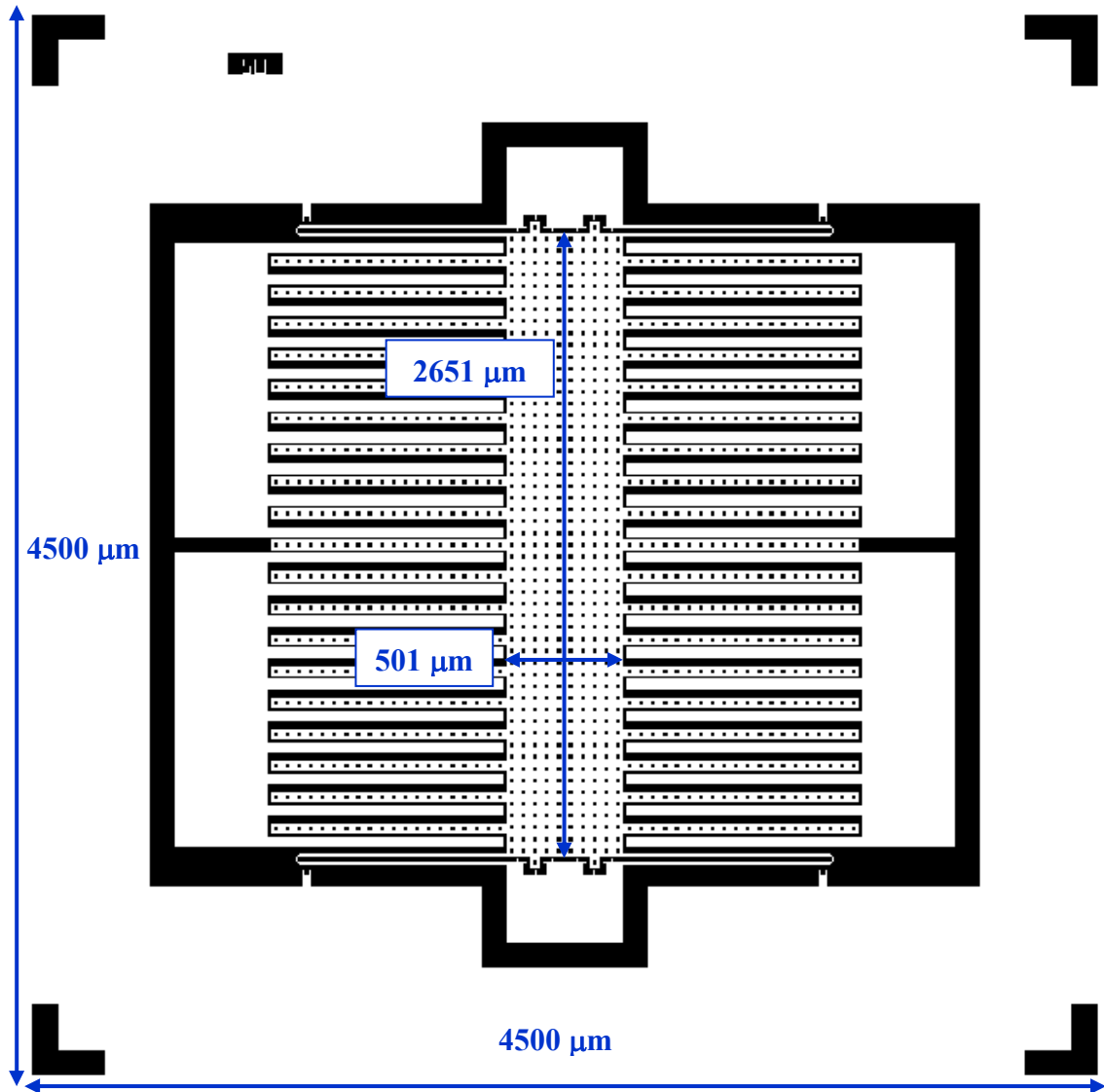
The primary recommendation for performing future experiments is to subject the MEMS shock test structures to a clean acceleration pulse with the smaller drop table. Cleaner acceleration pulses will help in avoiding failures caused by the high frequency content of acceleration pulses. Failures of MEMS shock test structures caused by ringing of acceleration pulses cannot be modeled with a dynamic code because it is impossible to detect exactly when the failure occurred. If the exact time of failure could be identified, then the proper time-pulse input for the dynamic code can be utilized. Once repeatable failures from cleaner pulses are achieved, ANSYS-LSDYNA can be used in modeling the failure stress to identify the failure strength. Furthermore, QinetiQ will have to design and fabricate additional parametric MEMS shock test structures that will reach critical stress levels with acceleration pulses that are smaller than 5000 g's to ensure failure from a cleaner pulse.

It would be advantageous to drop the UMD drop tower's table from various heights with various damping materials placed between the drop table and the base and record the acceleration pulses for performing FFT of the pulses. FFT of the recorded pulses will indicate the frequency content for each drop height, damping material and g-level. Thus

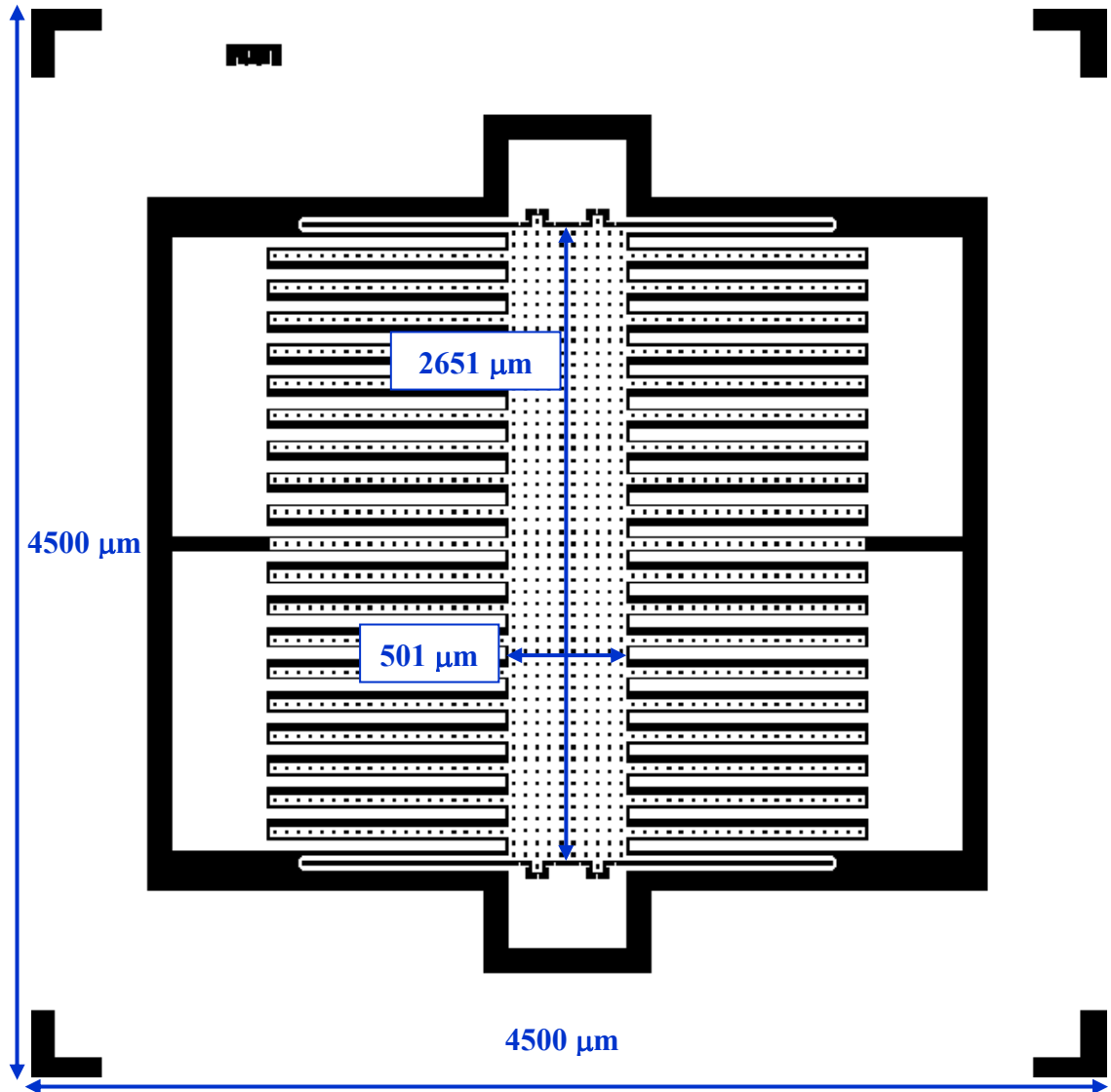
QinetiQ can design additional MEMS shock test structures that will reach critical stress levels with acceleration pulses and not fail due to resonance. Other recommendations are to continue preparing the samples in a cleanroom and to continue storing the test specimens inside zip-lock bags to keep the MEMS dies as free of dust as possible. However, the dies will still pick up some dust particles since the drop towers are not located in a cleanroom. The last few sets of sample bags were carefully bubble-wrapped because there were some failures of the dies even with careful handling (not included in the results), and bubble-wrapping helped in reducing the handling failures.

Appendix A: Accelerometer Drawings

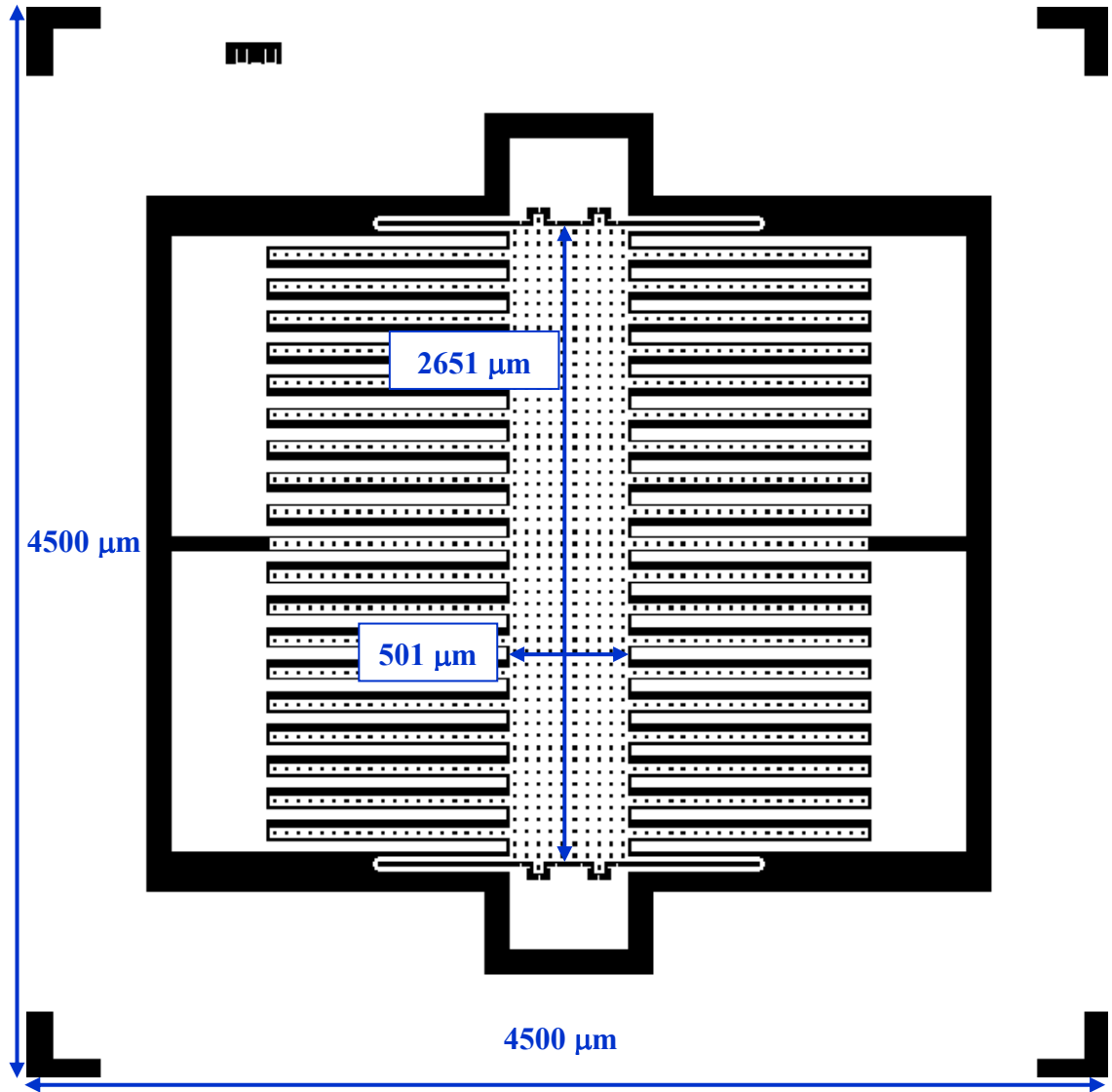
50g Accelerometer Overview



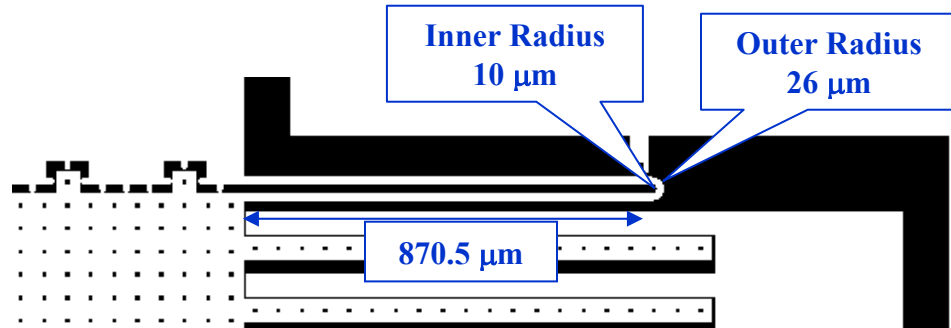
250g Accelerometer Overview



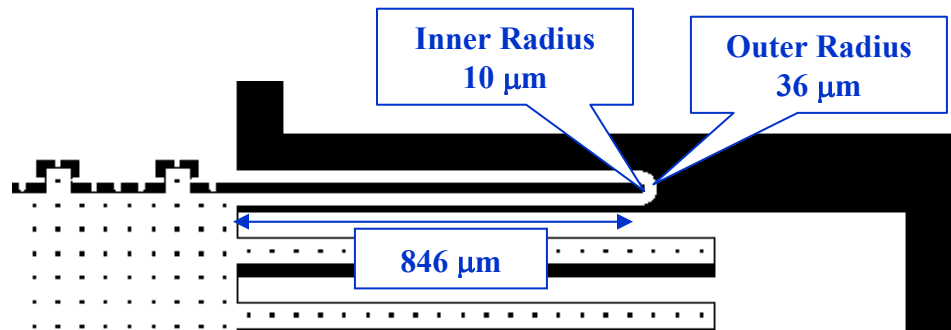
1000g Accelerometer Overview



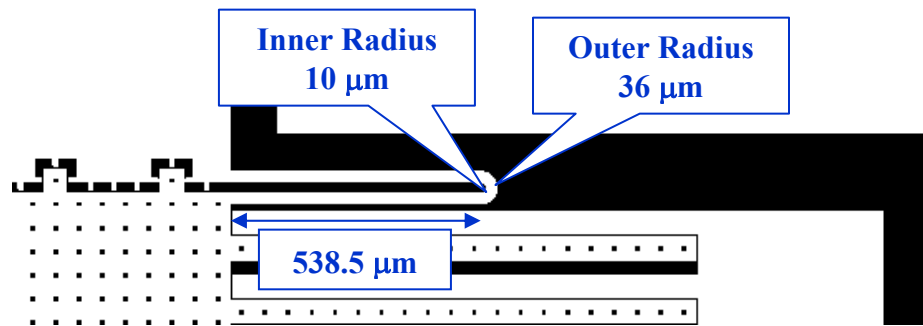
50g Accelerometer Spring



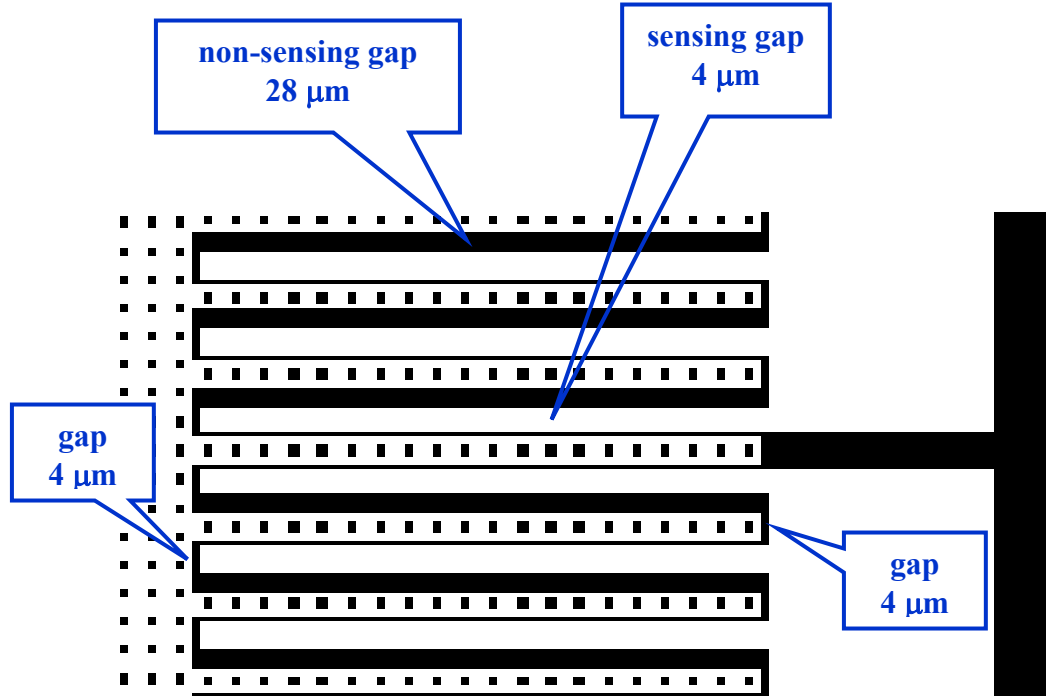
250g Accelerometer Spring



1000g Accelerometer Spring



Gaps



Appendix B: 4g Switch

The 4g switch die contains two switches; one switch is for horizontal (X) motion and the other is for vertical (Y) motion. Figure 27 shows a detailed view of a 4g switch die.

Every structure in a g switch except for the isolated contact pad is electrically connected.

When the proof mass makes contact with the electrically isolated contact pad, the switch closes. Similar to the accelerometers, the g switch proof mass has 9 micron \times 9 micron holes which allow quicker release of the proof mass. Also, the switch has mechanical and electrical stoppers that prevent over-ranging. Additionally, each proof mass has a tether that anchors the mass to the die. The tether is required during processing for successful fabrication of the switches, but it must be removed after fabrication to enable correct functionality of the switch because it significantly restricts the proof mass motion. As seen in Figure 28, a focused ion beam (FIB) was used to free one of the proof masses thus allowing testing of the free switch. Then the switch was subjected to ~ 5000 g's acceleration pulses along the 'X' and 'Z' directions, and no structural failures occurred.

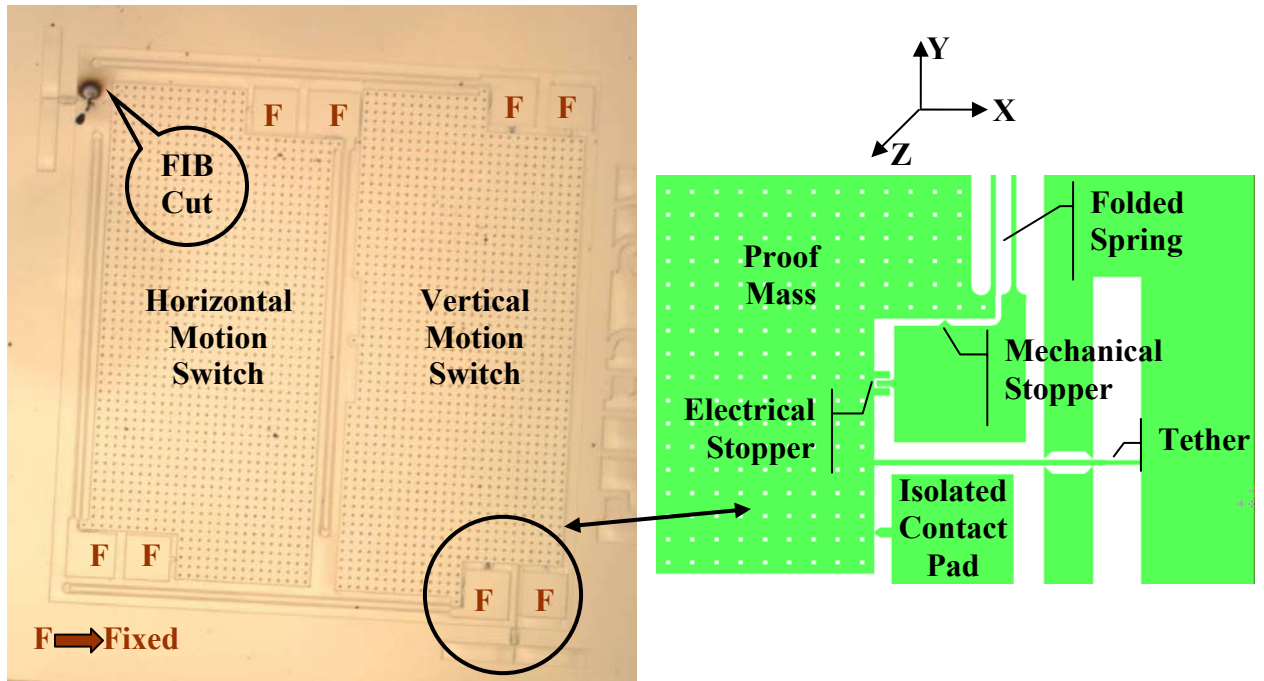


Figure 27: A detailed view of a 4g switch die

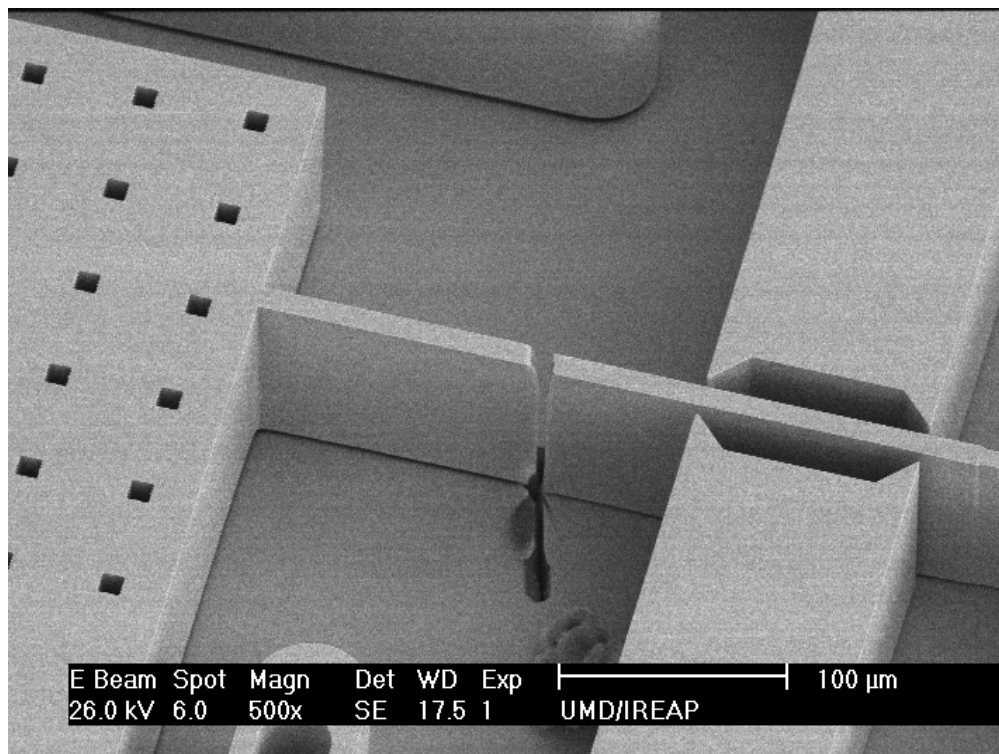


Figure 28: FIB cut of the tether frees the proof mass prior to testing

Appendix C: Analytical Stress Calculations

Analytical Calculations for Block 1 Test Structures

Axial Loading (Acceleration Along Positive X Direction)

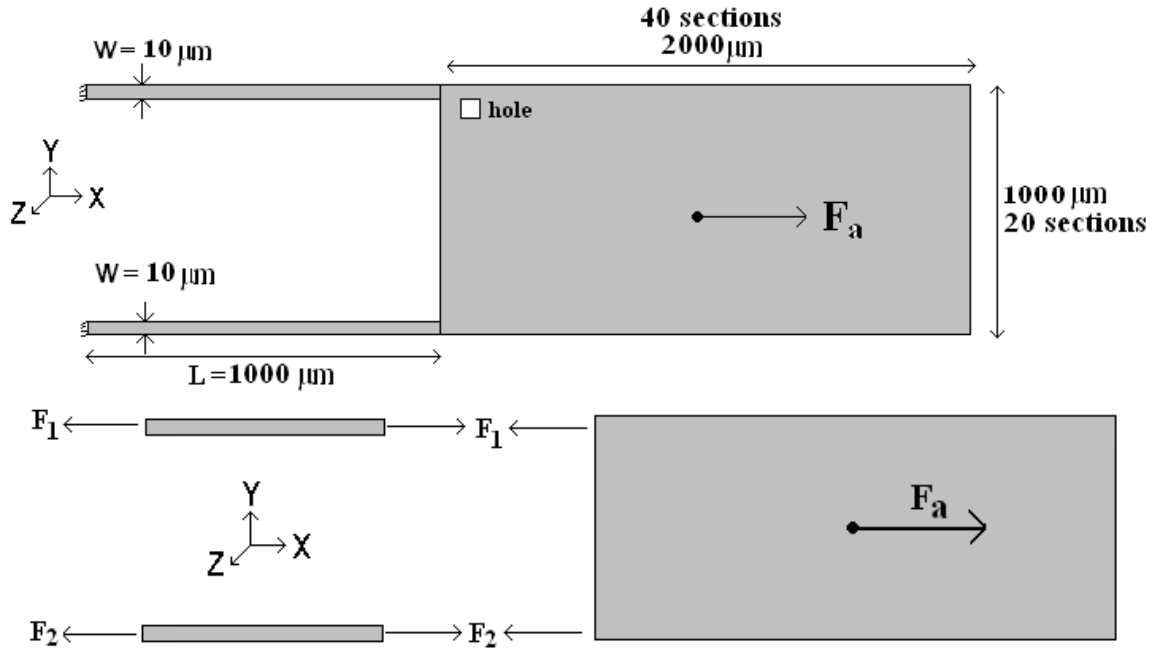


Figure 29: A Block 1 test structure and its free body diagram (axial loading)

Dimensions and Properties

Thickness of device layer (t) = $100\ \mu\text{m}$

Hole dimensions: $10\ \mu\text{m} \times 10\ \mu\text{m}$

Section dimensions: $50\ \mu\text{m} \times 50\ \mu\text{m}$

$W = 10\ \mu\text{m}$

$L = 1000\ \mu\text{m}$ (Type 1 – Type 4)

Young's Modulus (E) = $169\ \text{GPa}$

Density (ρ) = $2330\ \text{kg/m}^3$

Since all the Block 1 test structures have the same size cantilever beams and the same size proof mass, the axial stress for all four cases (Type 1 - Type 4) is the same. Figure 29 shows the free body diagram of a Block 1 structure subjected to acceleration along the positive X axis. Due to symmetric geometry and loading condition, $F_1 = F_2 = F_a/2$. The following steps illustrate axial stress determinations for the Block 1 test structures subjected to 5000g acceleration.

1. Determine the section mass

The dimensions of each section are $50\mu\text{m}$ by $50\mu\text{m}$, and each section includes a $10\mu\text{m}$ square hole.

$$\begin{aligned} \text{Section Mass} &= [\text{section area} - \text{hole area}](\rho)(t) \\ &= \left[(50\mu\text{m})^2 - (10\mu\text{m})^2 \right] \left(2330 \frac{\text{kg}}{\text{m}^3} \right) (100\mu\text{m}) = 5.592 * 10^{-10} \text{ kg} \end{aligned}$$

2. Find the applied force F_a

$$F_a = ma = \left[(5.592 * 10^{-10} \frac{\text{kg}}{\text{section}}) ((20 * 40) \text{ sections}) \right] \left[5,000 * 9.8 \frac{\text{m}}{\text{sec}^2} \right] = 0.0219 \text{ N}$$

3. Find the axial stress σ_x

$$\sigma_x = \frac{F_a/2}{\text{Cross Section Area}} = \frac{0.0219 \text{ N} / 2}{100\mu\text{m} * 10\mu\text{m}} = 0.0110 \text{ GPa}$$

In-Plane Bending (Acceleration Along Negative Y Direction)

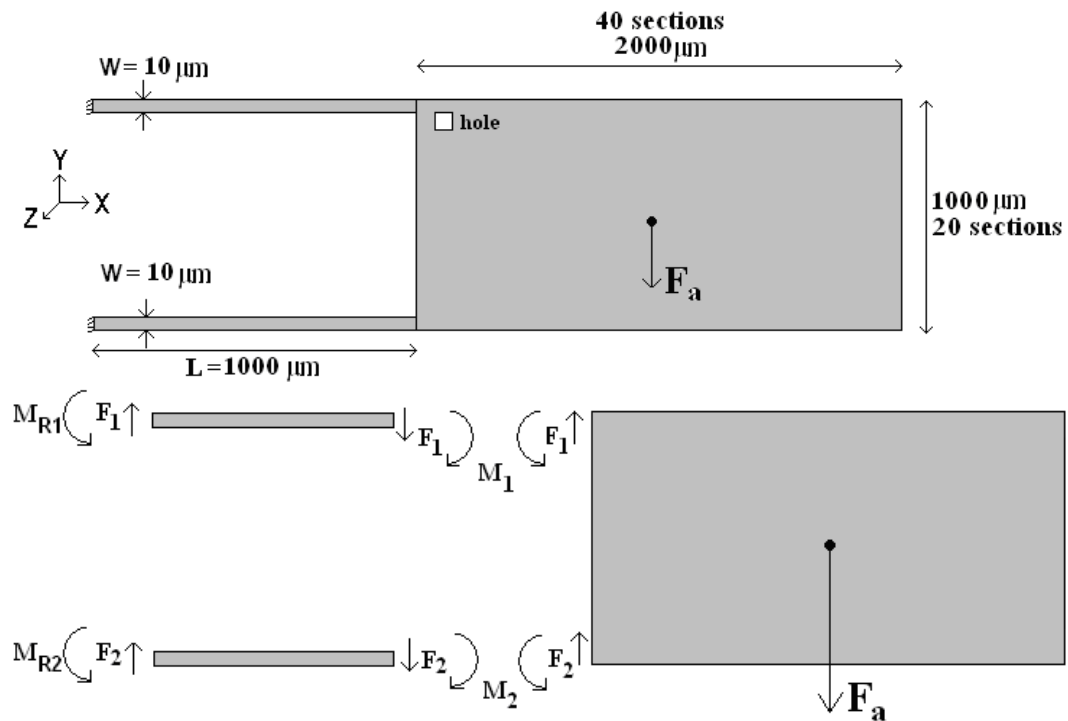


Figure 30: A Block 1 test structure and its free body diagram (in-plane bending)

Dimensions and Properties

Thickness of device layer (t) = $100\mu\text{m}$

Hole dimensions: $10\mu\text{m} \times 10\mu\text{m}$

Section dimensions: $50\mu\text{m} \times 50\mu\text{m}$

$W = 10\mu\text{m}$

$L = 1000\mu\text{m}$

Young's Modulus (E) = 169GPa

Density (ρ) = 2330kg/m^3

Since all the Block 1 test structures have the same size cantilever beams and the same size proof masses, the in-plane bending stress for all four cases (Type 1 - Type 4) is the

same. Figure 30 shows the free body diagram of a Block 1 structure subjected to acceleration along the negative Y axis. The following set of steps show the maximum stress calculation for Block 1 structures subjected to a 5000g acceleration along the negative Y direction:

1. Determine the section mass

The dimensions of each section are 50μm by 50μm, and each section includes a 10μm square hole.

$$\begin{aligned} \text{Section Mass} &= [\text{section area} - \text{hole area}](\rho)(t) \\ &= \left[(50\mu m)^2 - (10\mu m)^2 \right] \left(2330 \frac{\text{kg}}{\text{m}^3} \right) (100\mu m) = 5.592 * 10^{-10} \text{ kg} \end{aligned}$$

2. Find the applied force F_a

$$F_a = ma = \left[(5.592 * 10^{-10} \frac{\text{kg}}{\text{section}}) ((20 * 40) \text{ sections}) \right] \left[5,000 * 9.8 \frac{\text{m}}{\text{sec}^2} \right] = 0.0219 \text{ N}$$

3. Determine the force F_{a_max} that brings the proof mass in contact with side wall

The maximum allowable proof mass displacement in the Y direction is 5μm due to the side walls. If the structure is subjected to a 0.0219N force in the negative y direction and if there are no barrier walls, then the structure displaces 648μm in the negative y direction. The magnitude of this displacement was determined using ANSYS finite element analysis software. Since there is a 5μm gap between the proof mass and its surroundings, the following force would bring the structure in contact with the surroundings:

$$F_{a_max} = \frac{5\mu m}{648\mu m} * 0.0219 \text{ N} = 1.6914 * 10^{-4} \text{ N}$$

4. Determine the forces F_1 and F_2

Due to symmetry in geometry and loading

$$F_1 = F_2 = F_{a_max} / 2 = 1.6914 * 10^{-4} N / 2 = 8.4570 * 10^{-5} N$$

5. Find the moments M_1 and M_2

Due to symmetry in geometry and loading

$$\begin{aligned} M_1 = M_2 &= F_{a_max} / 2 * (2000 \mu m / 2) = F_a * 500 \mu m \\ &= 1.6914 * 10^{-4} N * 500 \mu m = 8.4570 * 10^{-8} N \cdot m \end{aligned}$$

6. Solve for the reaction moments: M_{R1} and M_{R2}

Due to symmetry in geometry and loading

$$\begin{aligned} M_{R1} = M_{R2} &= F_2 * L + M_2 \\ &= 8.4570 * 10^{-5} N * 1000 \mu m + 8.4570 * 10^{-8} N \cdot m = 1.6914 * 10^{-7} N \cdot m \end{aligned}$$

7. Find the Moment of Inertia (I_z) for the cantilever beams

$$I_z = \frac{1}{12} t w^3 = \frac{1}{12} (100 \mu m) (10 \mu m)^3 = 8.3333 * 10^{-21} m^4$$

8. Solve for the maximum stress σ_x (at the wall support)

$$\sigma_x = \frac{M_{R2}(t/2)}{I_z} = \frac{(1.6914 * 10^{-7} N \cdot m)(10 \mu m / 2)}{(8.3333 * 10^{-21} m^4)} = 0.1015 \text{ GPa}$$

Out-of-Plane Bending (Acceleration Along Positive Z Direction)

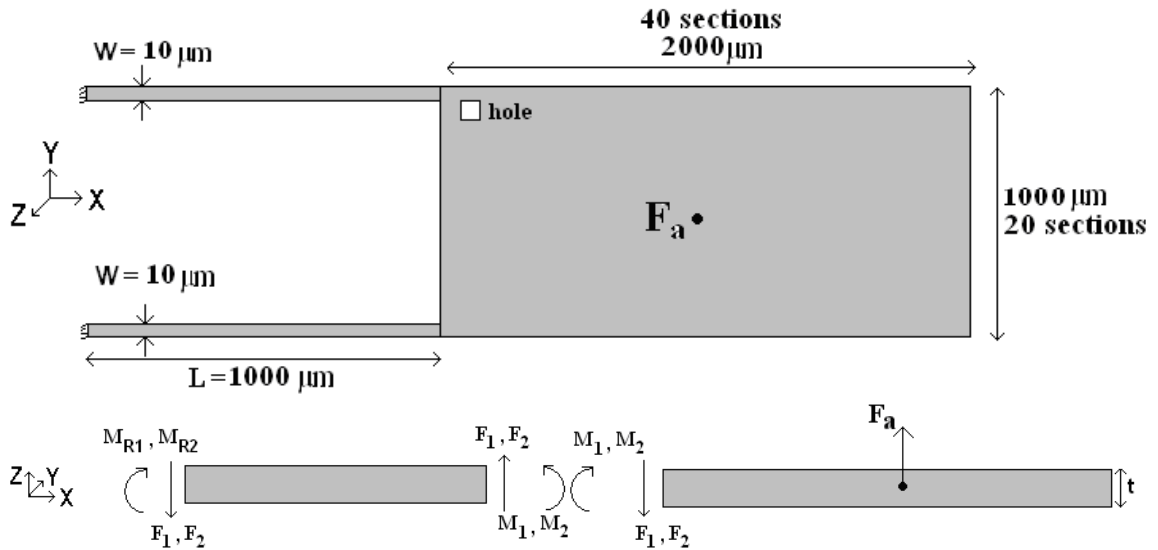


Figure 31: A Block 1 test structure and its free body diagram (out-of-plane bending)

Dimensions and Properties

Thickness of device layer (t) = $100\mu\text{m}$

Hole dimensions: $10\mu\text{m} \times 10\mu\text{m}$

Section dimensions: $50\mu\text{m} \times 50\mu\text{m}$

$W = 10\mu\text{m}$

$L = 1000\mu\text{m}$ (Type 1 – Type 4)

Young's Modulus (E) = 169GPa

Density (ρ) = 2330kg/m^3

Since all the Block 1 test structures have the same size cantilever beams and the same size proof masses, the out-of-plane bending stress for all four cases (Type 1 - Type 4) is the same. Figure 31 shows the free body diagram of a Block 1 structure subjected to acceleration along the positive Z axis. The following set of steps show the maximum

stress calculation for Block 1 structures subjected to a 5000g acceleration along positive Z direction:

1. Determine the section mass

The dimensions of each section are 50µm by 50µm, and each section includes a 10µm square hole.

$$\begin{aligned} \text{Section Mass} &= [\text{section area} - \text{hole area}](\rho)(t) \\ &= \left[(50\mu\text{m})^2 - (10\mu\text{m})^2 \right] \left(2330 \frac{\text{kg}}{\text{m}^3} \right) (100\mu\text{m}) = 5.592 * 10^{-10} \text{kg} \end{aligned}$$

2. Find the applied force F_a

$$F_a = ma = \left[\left(5.592 * 10^{-10} \frac{\text{kg}}{\text{section}} \right) (20 * 40 \text{ sections}) \right] \left[5,000 * 9.8 \frac{\text{m}}{\text{sec}^2} \right] = 0.0219N$$

3. Determine the forces F_1 and F_2

Due to symmetry in geometry and loading

$$F_1 = F_2 = F_a / 2 = 0.0219N / 2 = 0.0110N$$

4. Find the moments M_1 and M_2

Due to symmetry in geometry and loading

$$\begin{aligned} M_1 = M_2 &= F_a / 2 * (2000\mu\text{m} / 2) = F_a * 500\mu\text{m} \\ &= 0.0219N * 500\mu\text{m} = 1.0960 * 10^{-5} \text{N-m} \end{aligned}$$

5. Solve for the reaction moments: M_{R1} and M_{R2}

Due to symmetry in geometry and loading

$$\begin{aligned} M_{R1} = M_{R2} &= F_2 * L + M_2 \\ &= 0.0110N * 1000\mu\text{m} + 1.0960 * 10^{-5} \text{N-m} = 2.1921 * 10^{-5} \text{N-m} \end{aligned}$$

6. Find the Moment of Inertia (I_Y) for the cantilever beams

$$I_Y = \frac{1}{12} t^3 w = \frac{1}{12} (100 \mu m)^3 (10 \mu m) = 8.3333 * 10^{-19} m^4$$

7. Solve for the maximum stress σ_x (at the wall support)

$$\sigma_x = \frac{M_{R2}(t/2)}{I_Y} = \frac{(2.1921 * 10^{-5} \text{ N-m})(100 \mu m / 2)}{(8.3333 * 10^{-19} m^4)} = 1.3152 \text{ GPa}$$

Note: For each of the three axes, if the applied acceleration direction is changed from positive to negative or vice versa, the calculated stresses and displacements will have the same magnitude but opposite signs.

Analytical Calculations for Block 2 Test Structures

Axial Loading (Acceleration Along Positive X Direction)

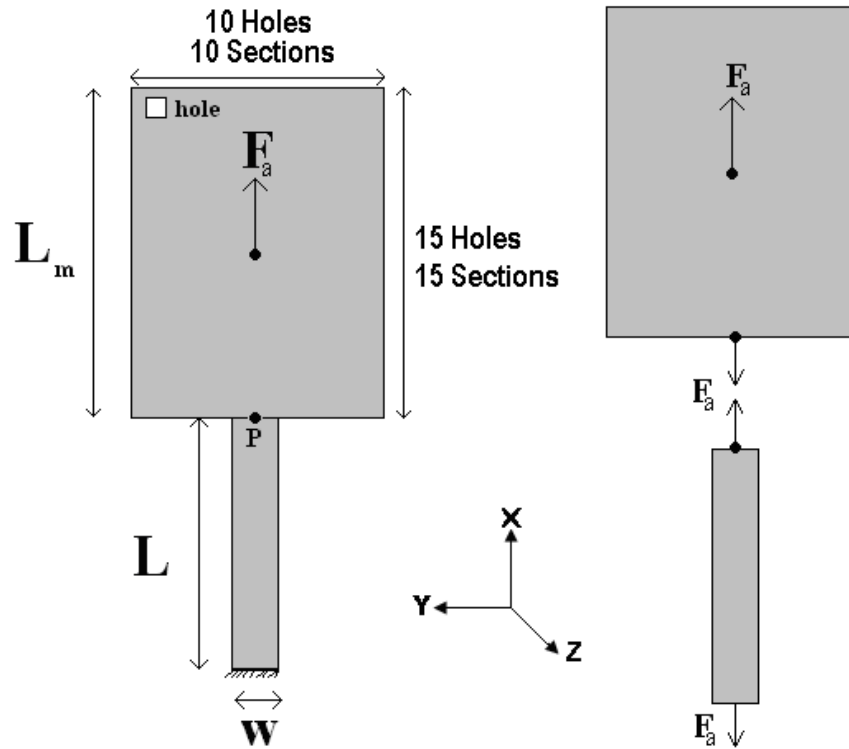


Figure 32: A Block 2 test structure and its free body diagram (axial loading)

Dimensions and Properties

Thickness of device layer (t) = $100\mu\text{m}$

Hole dimensions: $10\mu\text{m} \times 10\mu\text{m}$

Section dimensions: $50\mu\text{m} \times 50\mu\text{m}$

$W = 20\mu\text{m}$

$L = 100\mu\text{m}$ (Type 1), $200\mu\text{m}$ (Type 2), $300\mu\text{m}$ (Type 3)

Young's Modulus (E) = 169GPa

Density (ρ) = 2330kg/m^3

Since all the cantilevers have the same cross-sectional area and the same proof mass attached to the end, the axial stress for all three cases is the same. Figure 32 shows the free body diagram of a Block 2 structure subjected to acceleration along the positive X axis. The following steps illustrate axial stress determinations for the cantilevers subjected to 5000g acceleration.

1. Determine the section mass

The dimensions of each section are 50µm by 50µm, and each section includes a 10µm square hole.

$$\begin{aligned} \text{Section Mass} &= [\text{section area} - \text{hole area}](\rho)(t) \\ &= [(50\mu\text{m})^2 - (10\mu\text{m})^2] \left(2330 \frac{\text{kg}}{\text{m}^3} \right) (100\mu\text{m}) = 5.592 * 10^{-10} \text{kg} \end{aligned}$$

2. Find the applied force F_a

$$F_a = ma = \left[(5.592 * 10^{-10} \frac{\text{kg}}{\text{section}}) ((10 * 15) \text{sections}) \right] \left[5,000 * 9.8 \frac{\text{m}}{\text{sec}^2} \right] = 0.0041N$$

3. Find the axial stress σ_x

$$\sigma_x = \frac{F_a}{\text{Cross Section Area}} = \frac{0.0041N}{100\mu\text{m} * 20\mu\text{m}} = 0.00205GPa$$

In-Plane Bending (Acceleration Along Negative Y Direction)

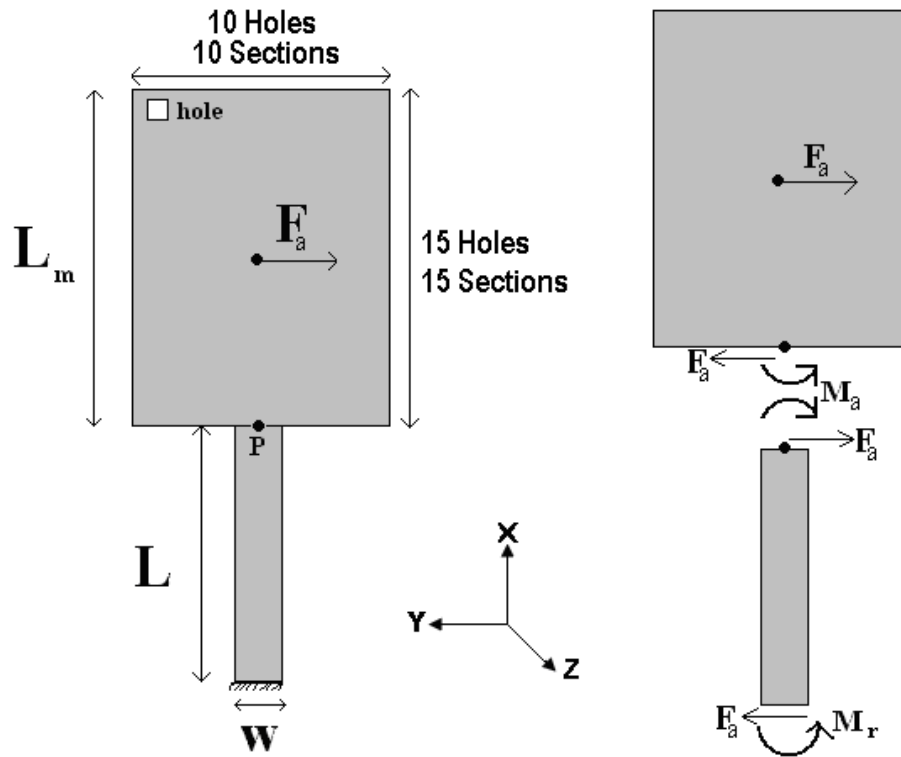


Figure 33: A Block 2 test structure and its free body diagram (in-plane bending)

Dimensions and Properties

Thickness of device layer (t) = $100\mu\text{m}$

Hole dimensions: $10\mu\text{m} \times 10\mu\text{m}$

Section dimensions: $50\mu\text{m} \times 50\mu\text{m}$

$W = 20\mu\text{m}$

$L = 100\mu\text{m}$ (Type 1), $200\mu\text{m}$ (Type 2), $300\mu\text{m}$ (Type 3)

Young's Modulus (E) = 169GPa

Density (ρ) = 2330kg/m^3

The following set of steps show a sample calculation for the structure in Figure 33 with a cantilever length of 300 μm subjected to 5000g acceleration:

1. Determine the section mass

The dimensions of each section are 50 μm by 50 μm , and each section includes a 10 μm square hole.

$$\begin{aligned} \text{Section Mass} &= [\text{section area} - \text{hole area}](\rho)(t) \\ &= \left[(50\mu\text{m})^2 - (10\mu\text{m})^2 \right] \left(2330 \frac{\text{kg}}{\text{m}^3} \right) (100\mu\text{m}) = 5.592 * 10^{-10} \text{kg} \end{aligned}$$

2. Find the applied force F_a

$$F_a = ma = \left[(5.592 * 10^{-10} \frac{\text{kg}}{\text{section}}) (10 * 15) \text{sections} \right] \left[5,000 * 9.8 \frac{\text{m}}{\text{sec}^2} \right] = 0.0041N$$

3. Find the moment M_a

$$M_a = F_a \left(\frac{1}{2} \right) (15 \text{sections}) (50 * 10^{-6} \text{m}) = 1.5413 * 10^{-6} \text{N-m}$$

4. Solve for the moment M_r

$$M_r = F_a \cdot L + M_a = (0.0041N \cdot 300\mu\text{m}) + 1.5413 * 10^{-6} \text{N-m} = 2.7743 * 10^{-6} \text{N-m}$$

5. Determine the moment of inertia I_z

$$I_z = \frac{w^3 t}{12} = \frac{(20\mu\text{m})^3 (100\mu\text{m})}{12} = 6.6667 * 10^{-20} \text{m}^4$$

6. Solve for the maximum stress σ_x (at the wall support)

$$\sigma_x = \frac{M_r (w/2)}{I_z} = \frac{(2.7743 * 10^{-6} \text{N-m}) (20\mu\text{m} / 2)}{(6.6667 * 10^{-20} \text{m}^4)} = 0.41615 \text{GPa}$$

7. Find the displacement of the cantilever

$$\begin{aligned}\delta_p &= -\left(\frac{F_a L^3}{3EI_z} + \frac{M_a L^2}{2EI_z}\right) \\ &= -\left(\frac{(0.0041N)(300\mu m)^3}{3(169GPa)(6.6667*10^{-20}m^4)} + \frac{(1.5413*10^{-6}N\cdot m)(300\mu m)^2}{2(169GPa)(6.6667*10^{-20}m^4)}\right) = -9.4393\mu m\end{aligned}$$

8. Find the slope Θ_p at point P

$$\begin{aligned}\theta_p &= -\left(\frac{F_a L^2}{2EI_z} + \frac{M_a L}{EI_z}\right) \\ &= -\left(\frac{(0.0041N)(300\mu m)^2}{2(169GPa)(6.6667*10^{-20}m^4)} + \frac{(1.5413*10^{-6}N\cdot m)(300\mu m)}{(169GPa)(6.6667*10^{-20}m^4)}\right) = -0.0575\text{rad}\end{aligned}$$

9. Find the maximum displacement of the proof mass

$$\begin{aligned}\delta_{proofmass} &= \delta_p + (15 \text{ sections} * 50\mu m) * \sin(\theta_p) \\ &= -9.4393 * 10^{-6} m + (15 * 50\mu m) * \sin(-0.0575) = -52.508\mu m\end{aligned}$$

Using the same method described in steps 1-9, the maximum stress and displacement of the proof mass were calculated in MATLAB. Table 13 shows these values for each of the three cantilever lengths subjected to 5000g acceleration.

Table 13: Maximum stress and displacement for cantilevers of various lengths L

Type	L (μm)	F (N)	M _r (N-m)	I _z (m ⁴)	σ _x (GPa)	δ _{proof mass} (μm)
1	100	0.0041	1.9523*10 ⁻⁶	6.6667*10 ⁻²⁰	0.2928	-12.433
2	200	0.0041	2.3633*10 ⁻⁶	6.6667*10 ⁻²⁰	0.3545	-29.696
3	300	0.0041	2.7743*10 ⁻⁶	6.6667*10 ⁻²⁰	0.4162	-52.508

MATLAB CODE (acceleration along negative Y direction)

```
% Batch 2 Devices
% Block 2 Devices

clc
```

```

clear

close all

rho = 2330; % kg/m^3
E = 169 * 10^9; % N/m^2
t = 100 * 10^-6; % Device Layer Thickness in m
a = 5000 * 9.8; % a = 5000 g in m/s^2

nl = 15; % # holes along X direction
nw = 10; % # holes along Y direction
block_length = 50 * 10^-6; % m
hole_length = 10 * 10^-6; % m
block_mass = ((block_length)^2 - (hole_length)^2) * rho * t; % kg
proof_mass = nl * nw * block_mass; % kg
L_m = nl * block_length; % m

F_a = proof_mass * a; % N
M_a = proof_mass * a * L_m/2; % N-m

L = 300 * 10^-6; % Length of cantilever in m (Type3)
% L = 200 * 10^-6 % Length of cantilever in m (Type2)
% L = 100 * 10^-6 % Length of cantilever in m (Type1)

w = 20 * 10^-6; % Width of cantilever in m
Iz = (1/12) * t * w^3; % m^4
M_r = F_a * L + M_a; % N-m

sigma_static = M_r * (w/2) / Iz; % N/m^2

```

```
theta_p = - F_a * L^2 / (2 * E * Iz) - M_a * L / (E * Iz);           % radians
delta_p = - F_a * L^3 / (3 * E * Iz) - M_a * L^2 / (2 * E * Iz);     % m
delta_proofmass_staitc = delta_p + L_m * sin(theta_p);              % m
```

Out-of-Plane Bending (Acceleration Along Negative Z Direction)

A Block 2 structure subjected to 5000g acceleration along the negative Z direction will require an analysis similar to the case of acceleration along the negative Y direction. The two changes necessary are to replace I_z with I_y and to use the appropriate distance from the neutral axis in the MATLAB code. Table 14 shows the values of the corresponding quantities for each of the three cantilever lengths.

Table 14: Maximum stress and displacement for cantilevers of various lengths L

Type	L (μm)	F (N)	M_r (N-m)	I_y (m^4)	σ_x (GPa)	$\delta_{\text{proof mass}}$ (μm)
1	100	0.0041	1.9523×10^{-6}	1.6667×10^{-18}	0.0586	-0.4973
2	200	0.0041	2.3633×10^{-6}	1.6667×10^{-18}	0.0709	-1.1880
3	300	0.0041	2.7743×10^{-6}	1.6667×10^{-18}	0.0832	-2.1013

MATLAB CODE (acceleration along '-Z' direction)

```
% Batch 2 Devices
```

```
% Block 2 Devices
```

```
clc
```

```
clear
```

```
close all
```

```
rho = 2330; % kg/m^3
```

```
E = 169 * 10^9; % N/m^2
```

```
t = 100 * 10^-6; % Device Layer Thickness in m
```

```
a = 5000 * 9.8; % a = 5000 g in m/s^2
```

```
nl = 15; % # holes along X direction
```

```

nw = 10; % # holes along Y direction
block_length = 50 * 10^-6; % m
hole_length = 10 * 10^-6; % m
block_mass = ((block_length)^2 - (hole_length)^2) * rho * t; % kg
proof_mass = nl * nw * block_mass; % kg
L_m = nl * block_length; % m

F_a = proof_mass * a; % N
M_a = proof_mass * a * L_m/2; % N-m

L = 300 * 10^-6; % Length of cantilever in m (Type3)
% L = 200 * 10^-6 % Length of cantilever in m (Type2)
% L = 100 * 10^-6 % Length of cantilever in m (Type1)

w = 20 * 10^-6; % Width of cantilever in m
Iy = (1/12) * t^3 * w; % m^4
M_r = F_a * L + M_a; % N-m

sigma_static = M_r * (t/2) / Iy; % N/m^2
theta_p = - F_a * L^2 / (2*E*Iy) - M_a * L / (E*Iy); % radians
delta_p = - F_a * L^3 / (3*E*Iy) - M_a * L^2 / (2*E*Iy); % m
delta_proofmass_staitc = delta_p + L_m * sin(theta_p); % m

```

Note: For each of the three axes, if the applied acceleration direction is changed from positive to negative or vice versa, the calculated stresses and displacements will have the same magnitude but opposite signs.

Analytical Calculations for Block 3 Test Structures

Axial Loading (Acceleration Along Positive X Direction)

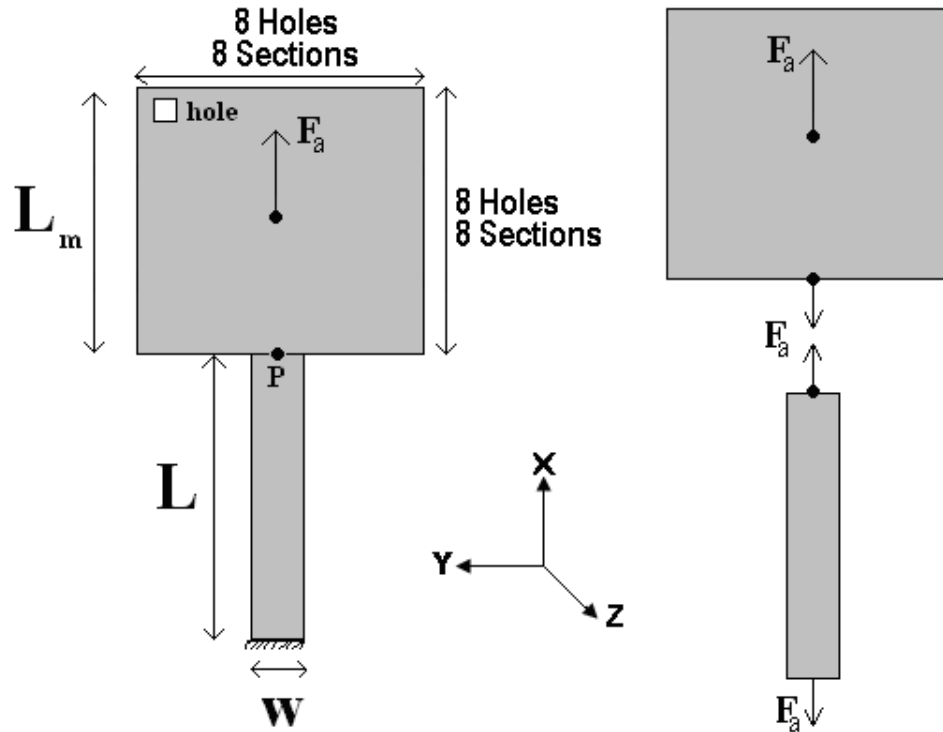


Figure 34: A Block 3 test structure and its free body diagram (axial loading)

Dimensions and Properties

Thickness of device layer (t) = $100\mu\text{m}$

Hole dimensions: $10\mu\text{m} \times 10\mu\text{m}$

Section dimensions: $50\mu\text{m} \times 50\mu\text{m}$

$W = 10\mu\text{m}$

$L = 100\mu\text{m}$ (Type 1), $200\mu\text{m}$ (Type 2), $300\mu\text{m}$ (Type 3), $400\mu\text{m}$ (Type 4)

Young's Modulus (E) = 169GPa

Density (ρ) = 2330kg/m^3

Since all the cantilevers have the same cross-sectional area and the same proof mass attached to the end, the axial stress for all four cases is the same. Figure 34 shows the free body diagram of a Block 3 structure subjected to acceleration along the positive X axis. The following steps illustrate axial stress determinations for the cantilevers subjected to 5000g acceleration.

1. Determine the section mass

The dimensions of each section are 50 μ m by 50 μ m, and each section includes a 10 μ m square hole.

$$\begin{aligned} \text{Section Mass} &= [\text{section area} - \text{hole area}](\rho)(t) \\ &= [(50\mu\text{m})^2 - (10\mu\text{m})^2] \left(2330 \frac{\text{kg}}{\text{m}^3} \right) (100\mu\text{m}) = 5.592 * 10^{-10} \text{kg} \end{aligned}$$

2. Find the applied force F_a

$$F_a = ma = \left[(5.592 * 10^{-10} \frac{\text{kg}}{\text{section}}) ((8 * 8) \text{sections}) \right] \left[5,000 * 9.8 \frac{\text{m}}{\text{sec}^2} \right] = 0.0018N$$

3. Find the axial stress σ_x

$$\sigma_x = \frac{F_a}{\text{Cross Section Area}} = \frac{0.0018N}{100\mu\text{m} * 10\mu\text{m}} = 0.0018GPa$$

In-Plane Bending (Acceleration Along Negative Y Direction)

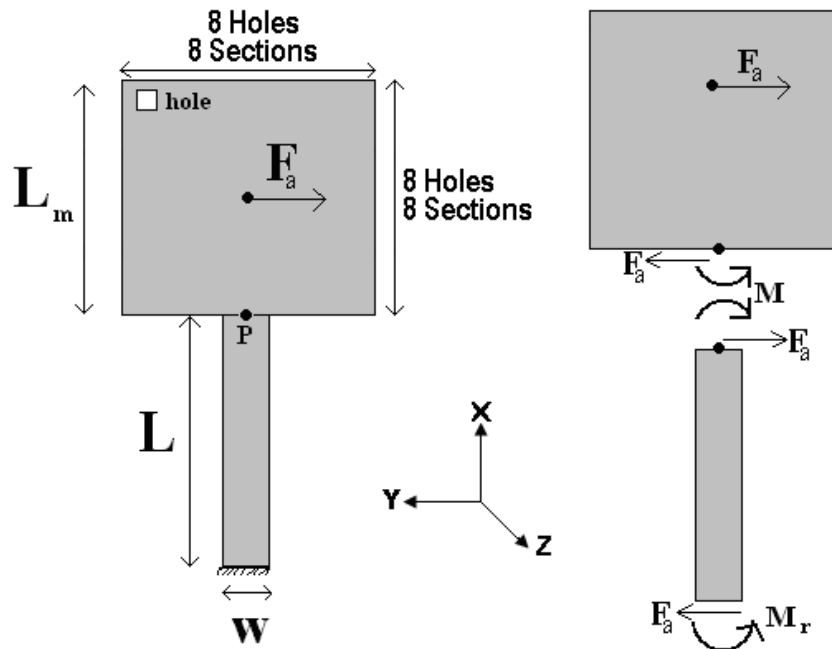


Figure 35: A Block 3 test structure and its free body diagram (in-plane bending)

Dimensions and Properties

Thickness of device layer (t) = $100\mu\text{m}$

Hole dimensions: $10\mu\text{m} \times 10\mu\text{m}$

Section dimensions: $50\mu\text{m} \times 50\mu\text{m}$

$W = 10\mu\text{m}$

$L = 100\mu\text{m}$ (Type 1), $200\mu\text{m}$ (Type 2), $300\mu\text{m}$ (Type 3), $400\mu\text{m}$ (Type 4)

Young's Modulus (E) = 169GPa

Density (ρ) = 2330kg/m^3

The following set of steps show a sample calculation for the structure in Figure 35 with a cantilever length of $300\mu\text{m}$ subjected to $5000g$ acceleration:

1. Determine the section mass

The dimensions of each section are $50\mu\text{m}$ by $50\mu\text{m}$, and each section includes a $10\mu\text{m}$ square hole.

$$\begin{aligned}\text{Section Mass} &= [\text{section area} - \text{hole area}](\rho)(t) \\ &= \left[(50\mu\text{m})^2 - (10\mu\text{m})^2 \right] \left(2330 \frac{\text{kg}}{\text{m}^3} \right) (100\mu\text{m}) = 5.592 * 10^{-10} \text{kg}\end{aligned}$$

2. Find the applied force F_a

$$F_a = ma = \left[(5.592 * 10^{-10} \frac{\text{kg}}{\text{section}}) ((8 * 8) \text{sections}) \right] \left[5,000 * 9.8 \frac{\text{m}}{\text{sec}^2} \right] = 0.0018 \text{N}$$

3. Find the moment M_a

$$M_a = F_a \left(\frac{1}{2} \right) (8 \text{sections}) (50 * 10^{-6} \text{m}) = 3.5073 * 10^{-7} \text{N-m}$$

4. Solve for the moment M_r

$$M_r = F_a \cdot L + M_a = (0.0018 \text{N} \cdot 300\mu\text{m}) + 3.5073 * 10^{-7} \text{N-m} = 8.7683 * 10^{-7} \text{N-m}$$

5. Determine the moment of inertia I_z

$$I_z = \frac{w^3 t}{12} = \frac{(10\mu\text{m})^3 (100\mu\text{m})}{12} = 8.3333 * 10^{-21} \text{m}^4$$

6. Solve for the maximum stress σ_x (at the wall support)

$$\sigma_x = \frac{M_r (w/2)}{I_z} = \frac{(8.7683 * 10^{-7} \text{N-m}) (10\mu\text{m} / 2)}{(8.3333 * 10^{-21} \text{m}^4)} = 0.5261 \text{GPa}$$

7. Find the displacement of the cantilever

$$\begin{aligned}\delta_p &= - \left(\frac{F_a L^3}{3EI_z} + \frac{M_a L^2}{2EI_z} \right) \\ &= - \left(\frac{(0.0018 \text{N}) (300\mu\text{m})^3}{3(169 \text{GPa}) (8.3333 * 10^{-21} \text{m}^4)} + \frac{(3.5073 * 10^{-7} \text{N-m}) (300\mu\text{m})^2}{2(169 \text{GPa}) (8.3333 * 10^{-21} \text{m}^4)} \right) = -22.4135 \mu\text{m}\end{aligned}$$

8. Find the slope Θ_p at point P

$$\theta_p = -\left(\frac{F_a L^2}{2EI_z} + \frac{M_a L}{EI_z}\right)$$

$$= -\left(\frac{(0.0018\text{N})(300\mu\text{m})^2}{2(169\text{GPa})(8.3333*10^{-21}\text{m}^4)} + \frac{(3.5073*10^{-7}\text{N-m})(300\mu\text{m})}{(169\text{GPa})(8.3333*10^{-21}\text{m}^4)}\right) = -0.1307\text{rad}$$

9. Find the maximum displacement of the proof mass

$$\delta_{proofmass} = \delta_p + (8 \text{ sections} * 50\mu\text{m}) * \sin(\theta_p)$$

$$= -22.4140 * 10^{-6} \text{ m} + (8 * 50\mu\text{m}) * \sin(-0.1307) = -74.5629\mu\text{m}$$

Using the same method described in steps 1-9, the maximum stress and displacement of the proof mass were calculated in MATLAB. Table 15 shows these values for each of the four cantilever lengths subjected to 5000g acceleration.

Table 15: Maximum stress and displacement for cantilevers of various lengths L

Type	L (μm)	F (N)	M_r (N-m)	I_z (m^4)	σ_x (GPa)	$\delta_{proof\ mass}$ (μm)
1	100	0.0018	$5.2610*10^{-7}$	$8.3333*10^{-21}$	0.3157	-14.1102
2	200	0.0018	$7.0146*10^{-7}$	$8.3333*10^{-21}$	0.4209	-38.1582
3	300	0.0018	$8.7683*10^{-7}$	$8.3333*10^{-21}$	0.5261	-74.5629
4	400	0.0018	$1.0522*10^{-6}$	$8.3333*10^{-21}$	0.6313	-125.6537

MATLAB CODE (acceleration along negative Y direction)

```
% Batch 2 Devices
% Block 3 Devices

clc
clear
close all

rho = 2330; % kg/m^3
```

```

E = 169 * 10^9; % N/m^2
t = 100 * 10^-6; % Device Layer Thickness in m
a = 5000 * 9.8; % a = 5000 g in m/s^2

nl = 8; % # holes along X direction
nw = 8; % # holes along Y direction
block_length = 50 * 10^-6; % m
hole_length = 10 * 10^-6; % m
block_mass = ((block_length)^2 - (hole_length)^2) * rho * t; % kg
proof_mass = nl * nw * block_mass; % kg
L_m = nl * block_length; % m

F_a = proof_mass * a; % N
M_a = proof_mass * a * L_m/2; % N-m

L = 400 * 10^-6; % Length of cantilever in m (Type4)
% L = 300 * 10^-6; % Length of cantilever in m (Type3)
% L = 200 * 10^-6; % Length of cantilever in m (Type2)
% L = 100 * 10^-6; % Length of cantilever in m (Type1)

w = 10 * 10^-6; % Width of cantilever in m
Iz = (1/12) * t * w^3; % m^4
M_r = F_a * L + M_a; % N-m
sigma_static = M_r * (w/2) / Iz; % N/m^2
theta_p = - F_a * L^2 / (2*E*Iz) - M_a * L / (E*Iz); % radians
delta_p = - F_a * L^3 / (3*E*Iz) - M_a * L^2 / (2*E*Iz); % m
delta_proofmass_staitc = delta_p + L_m * sin(theta_p); % m

```

Out-of-Plane Bending (Acceleration Along Negative Z Direction)

A Block 3 structure subjected to 5000g acceleration along the negative Z direction will require an analysis similar to the case of acceleration along the negative Y direction. The two changes necessary are to replace I_z with I_y and to use the appropriate distance from the neutral axis in the MATLAB code. Table 16 shows the values of the corresponding quantities for each of the four cantilever lengths.

Table 16: Maximum stress and displacement for cantilevers of various lengths L

Type	L (μm)	F (N)	M_r (N-m)	I_y (m^4)	σ_x (GPa)	$\delta_{\text{proof mass}}$ (μm)
1	100	0.0018	$5.2610 \cdot 10^{-7}$	$8.3333 \cdot 10^{-19}$	0.0316	-0.1411
2	200	0.0018	$7.0146 \cdot 10^{-7}$	$8.3333 \cdot 10^{-19}$	0.0421	-0.3819
3	300	0.0018	$8.7683 \cdot 10^{-7}$	$8.3333 \cdot 10^{-19}$	0.0526	-0.7471
4	400	0.0018	$1.0522 \cdot 10^{-6}$	$8.3333 \cdot 10^{-19}$	0.0631	-1.2618

MATLAB CODE (acceleration along negative Z direction)

```
% Batch 2 Devices
```

```
% Block 3 Devices
```

```
clc
```

```
clear
```

```
close all
```

```
rho = 2330; % kg/m^3
```

```
E = 169 * 10^9; % N/m^2
```

```
t = 100 * 10^-6; % Device Layer Thickness in m
```

```
a = 5000 * 9.8; % a = 5000 g in m/s^2
```

```
nl = 8; % # holes along X direction
```

```

nw = 8; % # holes along Y direction
block_length = 50 * 10^-6; % m
hole_length = 10 * 10^-6; % m
block_mass = ((block_length)^2 - (hole_length)^2) * rho * t; % kg
proof_mass = nl * nw * block_mass; % kg
L_m = nl * block_length; % m

F_a = proof_mass * a; % N
M_a = proof_mass * a * L_m/2; % N-m
L = 400 * 10^-6; % Length of cantilever in m (Type4)
% L = 300 * 10^-6; % Length of cantilever in m (Type3)
% L = 200 * 10^-6; % Length of cantilever in m (Type2)
% L = 100 * 10^-6; % Length of cantilever in m (Type1)

w = 10 * 10^-6; % Width of cantilever in m
Iy = (1/12) * t^3 * w; % m^4
M_r = F_a * L + M_a; % N-m

sigma_static = M_r * (t/2) / Iy; % N/m^2
theta_p = - F_a * L^2 / (2*E*Iy) - M_a * L / (E*Iy); % radians
delta_p = - F_a * L^3 / (3*E*Iy) - M_a * L^2 / (2*E*Iy); % m
delta_proofmass_staitc = delta_p + L_m * sin(theta_p); % m

```

Note: For each of the three axes, if the applied acceleration direction is changed from positive to negative or vice versa, the calculated stresses and displacements will have the same magnitude but opposite signs.

Table 17: Static stress summary for the MEMS shock test structures

Block	Length (μm)	Loading Direction	Static Stress (GPa)	Location
1	1000	Axial	0.0110	Along Cantilever
		In-Plane	0.1015	Wall Support
		Out-of-Plane	1.3152	Wall Support
2	100	Axial	0.0021	Along Cantilever
		In-Plane	0.2928	Wall Support
		Out-of-Plane	0.0586	Wall Support
	200	Axial	0.0021	Along Cantilever
		In-Plane	0.3545	Wall Support
		Out-of-Plane	0.0709	Wall Support
	300	Axial	0.0021	Along Cantilever
		In-Plane	0.4162	Wall Support
		Out-of-Plane	0.0832	Wall Support
3	100	Axial	0.0018	Along Cantilever
		In-Plane	0.3157	Wall Support
		Out-of-Plane	0.0316	Wall Support
	200	Axial	0.0018	Along Cantilever
		In-Plane	0.4209	Wall Support
		Out-of-Plane	0.0421	Wall Support
	300	Axial	0.0018	Along Cantilever
		In-Plane	0.5261	Wall Support
		Out-of-Plane	0.0526	Wall Support
	400	Axial	0.0018	Along Cantilever
		In-Plane	0.6313	Wall Support
		Out-of-Plane	0.0631	Wall Support

Appendix D: Shock Amplification Factor Calculations

According to Sloan [28], the shock amplification factors are defined as:

$$\text{Amp. Factor} = \frac{4 * f_n * T}{1 - 4 * (f_n * T)^2} * \cos(\pi * f_n * T), \quad f_n * T < 0.5 \quad \text{Eqn.1}$$

$$\text{Amp. Factor} = \frac{2 * f_n * T}{2 * f_n * T - 1} * \sin\left(\frac{2 * \pi}{2 * f_n * T + 1}\right), \quad 0.5 < f_n * T < 1.5 \quad \text{Eqn.2}$$

$$\text{Amp. Factor} = \frac{2 * f_n * T}{2 * f_n * T - 1} * \sin\left(\frac{4 * \pi}{2 * f_n * T + 1}\right), \quad 1.5 < f_n * T < 2.5 \quad \text{Eqn.3}$$

$$\text{Amp. Factor} ; 1, \quad f_n * T > 2.5 \quad \text{Eqn.4}$$

When Eqns.1 to 4 are plotted in Figure 36, it is observed that Eqn. 3 is invalid because of severe discontinuities with the other equations. Therefore, Eqn. 2 is used for the entire domain from 0.5 to 2.5. Results from the extended Eqn.2 are also plotted in Figure 36.

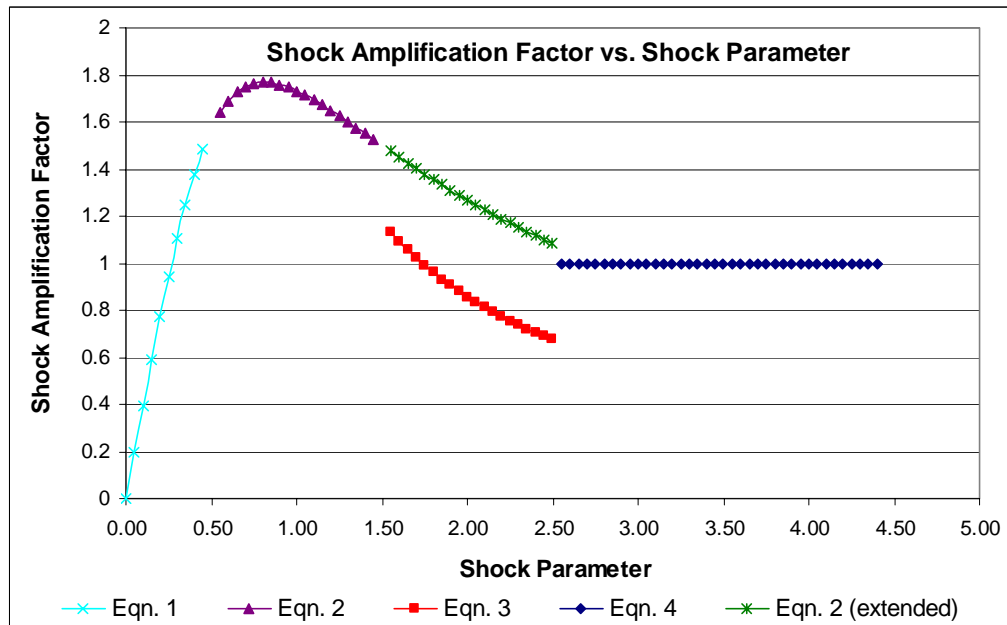


Figure 36: Shock amplification factor vs. shock parameter

Table 18 lists the shock amplification factors for Block 1, Block 2, and Block 3 structures that are calculated using Eqns. 1, 2 (extended), and 4 when subjected to 3000g and 5000g acceleration pulses.

Table 18: Shock amplification factor calculations

Block	Cantilever Length (μm)	3000g $f_n * T$	3000g Amp. Factor	5000g $f_n * T$	5000g Amp. Factor
1	1000	0.97	1.74	0.67	1.74
2	100	4.64	1.00	3.17	1.00
	200	3.04	1.00	2.07	1.24
	300	2.29	1.15	1.56	1.47
3	100	4.26	1.00	2.91	1.00
	200	2.61	1.00	1.78	1.36
	300	1.87	1.32	1.27	1.62
	400	1.43	1.54	0.98	1.74

References

- [1] Lehmann, G., Lomonosov, A. M., Hess, P., and Gumbsch, P., 2003, “Impulsive fracture of fused quartz and silicon crystals by nonlinear surface acoustic waves,” *Journal of Applied Physics*, **94**(5), pp. 2907-2914.
- [2] Hess, P., and Lomonosov, A. M., 2005, “Nanotechnological applications of nonlinear surface acoustic waves: Mechanism of brittle fracture,” *Applied Surface Science*, **248**, pp. 123–128.
- [3] Kozhushko, V. V., Lomonosov, A. M., and Hess, P., 2007, “Intrinsic Strength of Silicon Crystals in Pure- and Combined-Mode Fracture without Precrack,” *American Physical Society Physical Review Letters*, **98**(19), pp. 195505-1-4.
- [4] Ren, J., Orlov, S. S., and Hesselink, L., 2005, “Rear surface spallation on single-crystal silicon in nanosecond laser micromachining,” *Journal of Applied Physics*, **97**(10), pp. 104304-1-4.
- [5] Roundy, D., and Cohen, M. L., 2001, “Ideal strength of diamond, Si, and Ge,” *American Physical Society Physical Review B*, **64**(21), pp. 212103-1-3.
- [6] Brown, T. G., and Davis, B., 1998, “Dynamic high-g loading of MEMS sensors: ground and flight testing,” *SPIE Conference on Materials and Device Characterization in Micromachining*, Santa Clara, California, **3512**, pp. 228-235.
- [7] Brown, T. G., Davis, B., Hepner, D., Faust, J., Myers, C., Muller, P., Harkins, T., Hollis, M., Miller, C., and Placzankis, B., 2001, “Strap-Down Microelectromechanical (MEMS) Sensors for High-G Munition Applications,” *IEEE Transactions on Magnetics*, **37**(1), pp. 336-342.

- [8] Brown, T. G., 2003, "Harsh Military Environments and Microelectromechanical (MEMS) Devices," *Proceedings of IEEE Sensors*, **2**, pp. 753-760.
- [9] Davis, B. S., Denison, T., and Kaung, J., 2004, "A Monolithic High-g SOI-MEMS Accelerometer for Measuring Projectile Launch and Flight Accelerations," *Proceedings of IEEE Sensors*, **1**, pp. 296-299.
- [10] Davis, B. S., Denison, T., and Kaung, J., 2006, "A monolithic high-g SOI-MEMS accelerometer for measuring projectile launch and flight accelerations," *Shock and Vibration*, **13**(2), pp. 127-135.
- [11] Chen, K., Ayon, A., and Spearing, S. M., 2000, "Controlling and Testing the Fracture Strength of Silicon on the Mesoscale," *Journal of American Ceramic Society*, **83**(6), pp. 1476-1484.
- [12] Chen, K., Ayon, A., Zhang, X., and Spearing, S. M., 2002, "Effect of Process Parameters on the Surface Morphology and Mechanical Performance of Silicon Structures After Deep Reactive Ion Etching (DRIE)," *IEEE Journal of Microelectromechanical Systems*, **11**(3), pp. 264-275.
- [13] Yi, T., and Kim, C. J., 1999, "Microscale Material Testing: Etchant Effect on the Tensile Strength," *Transducers*, Sendai, Japan, pp. 518-521.
- [14] Yi, T., and Kim, C. J., 1999, "Measurement of mechanical properties for MEMS materials," *Measurement Science & Technology*, **10**, pp. 706-716.
- [15] Yi, T., Li, L., and Kim, C. J., 2000, "Microscale material testing of single crystal silicon: process effects on surface morphology and tensile strength," *Sensors and Actuators A: Physical*, **83**, pp. 172-178.

- [16] Namazu, T., Isono, Y., and Tanaka, T., 2000, "Nano-Scale Bending Test of Si Beam for MEMS", Proceedings of IEEE Thirteenth Annual Int. Conf. on Micro Electro Mechanical Systems, Miyazaki, Japan, pp. 205-210.
- [17] Namazu, T., Isono, Y., and Tanaka, T., 2000, "Evaluation of Size Effect on Mechanical Properties of Single Crystal Silicon by Nanoscale Bending Test Using AFM", IEEE Journal of Microelectromechanical Systems, **9**(4), pp. 450-459.
- [18] Hu, S. M., 1982, "Critical stress in silicon brittle fracture, and effect of ion implantation and other surface treatments," Journal of Applied Physics, **53**(5), pp. 3576-3580.
- [19] Suwito, W., Dunn, M. L., Cunningham, S. J., and Read, D. T., 1999, "Elastic moduli, strength, and fracture initiation at sharp notches in etched single crystal silicon microstructures," Journal of Applied Physics, **85**(7), pp. 3519-3534.
- [20] Berman, M., University of Maryland PhD. Proposal, 2006.
- [21] <http://www.empf.org/empfasis/june05/g0605.htm>, accessed March 24, 2008.
- [22] http://www.ccm.udel.edu/Pubs/posters02/P_posters/P-HighStrainRateTesting.jpg, accessed March 31, 2008
- [23] http://www.lansmont.com/Downloads/HighResPDF/Shock/Spec_Shock_15-D_Std_A_08_06.pdf, accessed March 24, 2008.
- [24] <http://www.epotek.com/SSCDocs/datasheets/353ND.PDF>, accessed April 13, 2008.
- [25] <http://www.epotek.com/SSCDocs/datasheets/930-4.PDF>, accessed April 13, 2008.
- [26] <http://www.epotek.com/SSCDocs/datasheets/H70E.PDF>, accessed April 13, 2008.

- [27] <http://www.epotek.com/SSCDocs/datasheets/H65-175MP.PDF>, accessed April 13, 2008.
- [28] Sloan, J. L., 1985, *Design and Packaging of Electronic Equipment*, Van Nostrand Reinhold Company, New York, NY, pp. 430-432.
- [29] Balachandran, B., and Magrab, E., 2004, *Vibrations*, Thomson, Belmont, CA.
- [30] Askeland, D. R., 1984, *The Science and Engineering of Materials*, Brooks/Cole Engineering Division, Wadsworth, Inc., Belmont, CA, pp.56-65.